Forecasting with importance-sampling and path-integrals: Applications to COVID-19

Lester Ingber[1]

Abstract:
Background: Forecasting nonlinear stochastic systems most often is quite difficult, without giving in to temptations to simply simplify models for the sake of permitting simple computations. **Objective**: Here, two basic algorithms, Adaptive Simulated Annealing (ASA) and path-integral codes PATHINT/PATHTREE (and their quantum generalizations qPATHINT/qPATHTREE) are described as being useful to detail such systems. **Method**: ASA and PATHINT/PATHTREE have been demonstrated as being effective to forecast properties in three disparate disciplines in neuroscience, financial markets, and combat analysis. Applications are described for COVID-19. **Results**: Not only can selected systems in these three disciplines be aptly modeled, but results of detailed calculations have led to new results and insights not previously obtained. **Conclusion**: While optimization and path-integral algorithms are now quite well-known (at least to many scientists), these applications give strong support to a quite generic application of these tools to stochastic nonlinear systems.

Key words: path integral; importance sampling; neuroscience; financial markets; combat analysis; COVID-19

1 Introduction

This paper describes the application of two basic algorithms to fairly generic issues in forecasting.

> (a) Adaptive Simulated Annealing (ASA) is an importance-sampling optimization code usually used for nonlinear, nonequilibrium, non-stationary, multivariate systems.
>
> (b) PATHINT is a numerical path-integral PATHINT code used for propagation of nonlinear probability distributions, including discontinuities.

These codes were developed by the author and applied across multiple disciplines.

There is not "one size fits all" in forecasting different systems. This is demonstrated below for three selected example systems. The author has addressed multiple projects across multiple disciplines using these tools. It is reasonable to expect that this approach can be applied to many future projects.

1.1 Technical considerations

If there is not time to process large data sets, then the data can be randomly sampled, e.g., as described in the "Developing bid-ask probabilities for high-frequency trading" sub-section below.

If the required forecast is longer than the conditional distribution can sustain, PATHINT/PATHTREE can be used to propagate the distribution.

---

[1] Corresponding author: Lester Ingber
email: lester@ingber.com or ingber@caa.caltech.edu
Additional information may be obtained at https://www.ingber.com.

The dataset should be broken into independent Training and Testing subsets, to test the trained distribution. If this is not possible, e.g., because of data or time limitations, at the least experts can be used to judge if the model is ready for real-time applications, e.g., the Delphi method (Okoli & Pawlowski, 2004).

1.2 Outline

Section 2 describes the ASA algorithm. If an algorithm is to be used across a large class of problems, then it must be tunable to different classes. Over the 30+ years of ASA development, the author has worked with many volunteers who have contributed valuable ideas, modifications and corrections to this code. This has resulted in over 150 ASA options that can be used for additional timing additional tuning making it useful across many classes of problems.

Section 3 describes the path integral algorithm and its mathematical equivalents, a large class of stochastic differential equations and a large class of partial differential equations. The advantages of the path integral algorithm are:

(a) intuitive description in terms of classical forces, inertia, momentum, etc., leading to new indicators.

(b) delivering a cost function derived from a Lagrangian, or its Action (Lagrangian x dt). Sometimes constraints need to be added as Lagrange multipliers, as was required for normalization requirements in financial risk projects (Ingber, 2010a).

This is followed by 3 Sections of applications. Section 4 discusses Statistical Mechanics of Neocortical Interactions (SMNI). Section 5 discusses Statistical Mechanics of Financial Markets (SMFM). Section 6 discusses Statistical Mechanics of Combat (SMC). Section 7 describes possible applications to forecosting the spread of COVID-19. Section 8 is the Conclusion.

1.3 Model of models (MOM)

It is likely that this work is competing with many others proposing neural-network (NN) approaches to forecasting, and therefore this must be addressed. The author has participated in NN research, applying ASA to optimize weights, and am aware of its strengths (Atiya *et al.*, 2003).

Neural networks and their use with Deep Learning (DL) have demonstrated great advances since a couple of decades ago when they fell out of favor because of their risks of not keeping current with changes of contexts of markets. This fear is still present and well-founded. The author has proposed an approach of Model of Models (MOM) to address this problem,

Forecasting benefits with audit trails back to basic assumptions, which is what a modeling approach offers. Deep Learning (DL) has invigorated AI approaches to parsing data in complex systems, often to develop control processes of these systems. A couple of decades ago, Neural Net AI approaches fell out of favor when concerns were apparent that such approaches offered little guidance to explain the ”why” or ”how” such algorithms worked to process data, e.g., contexts which was deemed important to deal with future events and outliers, etc.

The success of DL has overshadowed these concerns. However, that should not diminish their importance, especially if such systems are placed in positions to affect lives and human concerns. Humans ultimately must be responsible for structures they build.

An approach to dealing with these concerns can be called Model of Models (MOM). An argument in favor of MOM is that humans over thousands of years have developed models of reality across many disciplines, e.g., ranging over Physics, Biology, Mathematics, Economics, etc.

DL could be to process data for a given system in terms of a collection of models, and again to process the models over the same data to determine a superior model of models (MOM). Eventually, large DL (quantum) machines could possess a database of hundreds or thousands of models across many disciplines, and directly find the best (hybrid) MOM for a given system.

ASA can be used in the expanded context of MOM. This is suggested as a first step in a new discipline to which MOM is to be applied, to help develop a range of parameters useful for DL, as DL by itself may get stuck in non-ideal local minima of the importance-sampled space.

After a reasonable range of models is found, then DL permits much more efficient and accurate development of MOM for a given discipline/system.

2 Adaptive Simulated Annealing (ASA)

A paper discusses ASA in more detail (Ingber, 2012a).

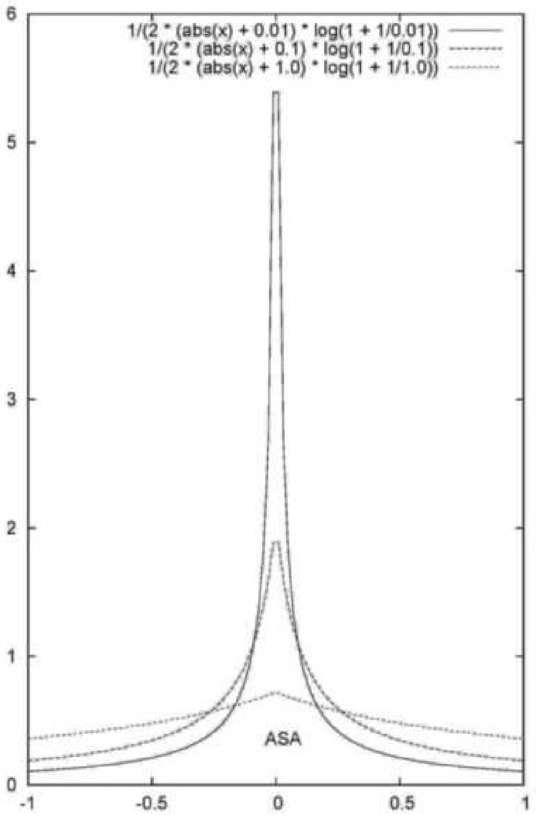

Fig. 1. The ASA distribution is shown at various "temperatures". Note that the effective tails range from quite wide to quite narrow.

Simulated annealing (SA) presents an optimization technique that can: (a) process cost functions possessing quite arbitrary degrees of nonlinearities, discontinuities, and stochasticity; (b) process quite arbitrary boundary conditions and constraints imposed on these cost functions; (c) be implemented quite easily with the degree of coding quite minimal relative to other nonlinear optimization algorithms; (d) statistically guarantee finding an optimal solution.

Adaptive Simulated Annealing (ASA) is a C-language code that finds the best global fit of a nonlinear cost-function over a D-dimensional space. The basic algorithm was originally published as Very Fast Simulated Reannealing (VFSR) in 1989 (Ingber, 1989a), after two years of application on combat simulations for the US Navy and Army. The code (Ingber, 1993a) can be used at no charge and downloaded from http://www.ingber.com/#ASA with mirrors at:
http://alumni.caltech.edu/ ingber
http://asa-caltech.sourceforge.net
https://code.google.com/p/adaptive-simulated-annealing .

ASA has over 100 OPTIONS to provide robust tuning over many classes of nonlinear stochastic systems. The current number is 152. These many OPTIONS help ensure that ASA can be used robustly across many classes of systems.

The "QUENCHing" OPTIONS are among the most important for controlling Adaptive Simulated Annealing. Fuzzy ASA algorithms in particular offer new ways of controlling how these QUENCHing OPTIONS may be applied across many classes of problems.

2.1 Theoretical foundations of adaptive simulated annealing (ASA)

The unique aspect of simulated annealing (SA) is its property of (weak) ergodicity, permitting such code to statistically and reasonably sample a parameter space. Note that for very large systems, ergodicity is not an entirely rigorous concept when faced with the real task of its computation (Ma, 1985). “Ergodic” is used in a very weak sense, as it is not proposed, theoretically or practically, that all states of the system are actually to be visited.

2.1.1 “Standard” simulated annealing (SA)

The Metropolis Monte Carlo integration algorithm (Metropolis *et al.*, 1953) was generalized by the Kirkpatrick algorithm to include a temperature schedule for efficient searching (Kirkpatrick *et al.*, 1983), usually referred to as Boltzmann annealing (BA). A sufficiency proof was then shown to put an lower bound on that schedule as $1/\log(t)$, where t is an artificial time measure of the annealing schedule (Geman & Geman, 1984). However, independent credit usually goes to several other authors for independently developing the algorithm that is now recognized as simulated annealing (Cerny, 1982; Pincus, 1970). XXX

2.1.2 Boltzmann annealing (BA)

Credit for the first simulated annealing is generally recognized as a Monte Carlo importance-sampling technique for doing large-dimensional path integrals arising in statistical physics problems (Metropolis *et al.*, 1953). This method was generalized to fitting non-convex cost-functions arising in a variety of problems, e.g., finding the optimal wiring for a densely wired computer chip (Kirkpatrick *et al.*, 1983). The choices of probability distributions described in this section are generally specified as Boltzmann annealing (BA) (Szu & Hartley, 1987).

The method of simulated annealing consists of three functional relationships.

1. $g(x)$: Probability density of state-space of D parameters $x = \{x^i; i = 1, D\}$.
2. $h(\Delta E)$: Probability for acceptance of new cost-function given the just previous value.
3. $T(k)$: schedule of “annealing” the “temperature” T in annealing-time steps k, i.e., of changing the volatility or fluctuations of one or both of the two previous probability densities.

The acceptance probability is based on the chances of obtaining a new state with “energy” E_{k+1} relative to a previous state with “energy” E_k,

$$\begin{aligned} h(\Delta E) &= \frac{\exp(-E_{k+1}/T)}{\exp(-E_{k+1}/T) + \exp(-E_k/T)} \\ &= \frac{1}{1 + \exp(\Delta E/T)} \\ &\approx \exp(-\Delta E/T), \end{aligned} \tag{1}$$

where ΔE represents the “energy” difference between the present and previous values of the energies (considered here as cost functions) appropriate to the physical problem, i.e., $\Delta E = E_{k+1} - E_k$. This essentially is the Boltzmann distribution contributing to the statistical mechanical partition function of the system (Binder & Stauffer, 1985).

This can be described by considering: a set of states labeled by x, each with energy $e(x)$; a set of probability distributions $p(x)$; and the energy distribution per state $d\big(e(x)\big)$, giving an aggregate energy E,

$$\sum_x p(x) d\big(e(x)\big) = E. \tag{2}$$

The principle of maximizing the entropy, S,

$$S = -\sum_x p(x) \ln[p(x)/p(\bar{x})], \tag{3}$$

where $\bar{x}$ represents a reference state, using Lagrange multipliers (Mathews & Walker, 1970) to constrain the energy to average value T, leads to the most likely Gibbs distribution $G(x)$,

$$G(x) = \frac{1}{Z} \exp\big(-H(x)/T\big), \tag{4}$$

in terms of the normalizing partition function Z, and the Hamiltonian H operator as the "energy" function,

$$Z = \sum_x \exp\big(-H(x)/T\big). \tag{5}$$

For such distributions of states and acceptance probabilities defined by functions such as $h(\Delta E)$, the equilibrium principle of detailed balance holds. I.e., the distributions of states before, $G(x_k)$, and after, $G(x_{k+1})$, applying the acceptance criteria, $h(\Delta E) = h(E_{k+1} - E_k)$ are the same:

$$G(x_k) h\big(\Delta E(x)\big) = G(x_{k+1}). \tag{6}$$

This is sufficient to establish that all states of the system can be sampled, in theory. However, the annealing schedule interrupts equilibrium every time the temperature is changed, and so, at best, this must be done carefully and gradually.

An important aspect of the SA algorithm is to pick the ranges of the parameters to be searched. In practice, computation of continuous systems requires some discretization, so without loss of much generality for applications described here, the space can be assumed to be discretized. There are additional constraints that are required when dealing with generating and cost functions with integral values. Many practitioners use novel techniques to narrow the range as the search progresses. For example, based on functional forms derived for many physical systems belonging to the class of Gaussian-Markovian systems, one could choose an algorithm for g,

$$g(\Delta x) = (2\pi T)^{-D/2} \exp[-\Delta x^2/(2T)], \tag{7}$$

where $\Delta x = x - x_0$ is the deviation of x from x_0 (usually taken to be the just-previously chosen point), proportional to a "momentum" variable, and where T is a measure of the fluctuations of the Boltzmann distribution g in the D-dimensional x-space. Given $g(\Delta x)$, it has been proven (Geman & Geman, 1984) that it suffices to obtain a global minimum of $E(x)$ if T is selected to be not faster than

$$T(k) = \frac{T_0}{\ln k}, \tag{8}$$

with T_0 "large enough."

doi:10.20944/preprints202009.0385.v2

A heuristic demonstration shows that this equation for T can suffice to give a global minimum of $E(x)$ (Szu & Hartley, 1987). In order to statistically assure, i.e., requiring many trials, that any point in x-space can be sampled infinitely often in annealing-time (IOT), it suffices to prove that the products of probabilities of not generating a state x IOT for all annealing-times successive to k_0 yield zero,

$$\prod_{k=k_0}^{\infty} (1 - g_k) = 0. \tag{9}$$

This is equivalent to

$$\sum_{k=k_0}^{\infty} g_k = \infty. \tag{10}$$

The problem then reduces to finding $T(k)$ to satisfy this equation.

For BA, if $T(k)$ is selected to be the Boltzmann criteria above, then the generating distribution g above gives

$$\sum_{k=k_0}^{\infty} g_k \geq \sum_{k=k_0}^{\infty} \exp(-\ln k) = \sum_{k=k_0}^{\infty} 1/k = \infty. \tag{11}$$

Although there are sound physical principles underlying the choices of the Boltzmann criteria above (Metropolis *et al.*, 1953), it was noted that this method of finding the global minimum in x-space was not limited to physics examples requiring Rather, this methodology can be readily extended to any problem for which a reasonable probability density $h(\Delta x)$ can be formulated (Kirkpatrick *et al.*, 1983).

2.1.3 Fast annealing (FA)

Although there are many variants and improvements made on the "standard" Boltzmann algorithm described above, many textbooks finish just about at this point without going into more detail about other algorithms that depart from this explicit algorithm (vanLaarhoven & Aarts, 1987). Specifically, it was noted that the Cauchy distribution has some definite advantages over the Boltzmann form (Szu & Hartley, 1987). The Cauchy distribution,

$$g(\Delta x) = \frac{T}{(\Delta x^2 + T^2)^{(D+1)/2}}, \tag{12}$$

has a "fatter" tail than the Gaussian form of the Boltzmann distribution, permitting easier access to test local minima in the search for the desired global minimum.

It is instructive to note the similar corresponding heuristic demonstration, that the Cauchy $g(\Delta x)$ statistically finds a global minimum. If the Boltzmann T is replaced by

$$T(k) = \frac{T_0}{k}, \tag{13}$$

then here

$$\sum_{k_0}^{\infty} g_k \approx \frac{T_0}{\Delta x^{D+1}} \sum_{k_0}^{\infty} \frac{1}{k} = \infty. \tag{14}$$

Note that the "normalization" of g has introduced the annealing-time index k, giving some insights into how to construct other annealing distributions. The method of FA is thus seen to have an annealing schedule exponentially faster than the method of BA. This method has been tested in a variety of problems (Szu & Hartley, 1987).

2.1.4 Adaptive simulated annealing (ASA)

In a variety of physical problems there is a D-dimensional parameter-space. Different parameters have different finite ranges, fixed by physical considerations, and different annealing-time-dependent sensitivities, measured by the derivatives of the cost-function at local minima. BA and FA have distributions that sample infinite ranges, and there is no provision for considering differences in each parameter-dimension; e.g., different sensitivities might require different annealing schedules. This prompted the development of a new probability distribution to accommodate these desired features (Ingber, 1989a), leading to a variant of SA that in fact justifies an exponential temperature annealing schedule. These are among several considerations that gave rise to Adaptive Simulated Annealing (ASA). Full details are available by obtaining the publicly available source code (Ingber, 1993a).

ASA considers a parameter α_k^i in dimension i generated at annealing-time k with the range

$$\alpha_k^i \in [A_i, B_i], \tag{15}$$

calculated with the random variable y^i,

$$\alpha_{k+1}^i = \alpha_k^i + y^i (B_i - A_i),$$

$$y^i \in [-1, 1]. \tag{16}$$

Define the generating function

$$g_T(y) = \prod_{i=1}^{D} \frac{1}{2(|y^i| + T_i)\,\ln(1 + 1/T_i)} \equiv \prod_{i=1}^{D} g_T^i(y^i). \tag{17}$$

Its cumulative probability distribution is

$$G_T(y) = \int_{-1}^{y^1} \dots \int_{-1}^{y^D} dy'^1 \dots dy'^D \, g_T(y') \equiv \prod_{i=1}^{D} G_T^i(y^i),$$

$$G_T^i(y^i) = \frac{1}{2} + \frac{\mathrm{sgn}\,(y^i)}{2} \frac{\ln(1 + |y^i|/T_i)}{\ln(1 + 1/T_i)}. \tag{18}$$

y^i is generated from a u^i from the uniform distribution

$$u^i[0, 1],$$

$$y^i = \mathrm{sgn}\,(u^i - \frac{1}{2}) T_i [(1 + 1/T_i)^{|2u^i - 1|} - 1]. \tag{19}$$

It is straightforward to calculate that for an annealing schedule for T_i

$$T_i(k) = T_{0i} \exp(-c_i k^{1/D}), \tag{20}$$

a global minima statistically can be obtained. I.e.,

$$\sum_{k_0}^{\infty} g_k \approx \sum_{k_0}^{\infty} [\prod_{i=1}^{D} \frac{1}{2|y^i|c_i}] \frac{1}{k} = \infty. \tag{21}$$

It seems sensible to choose control over c_i, such that

$$T_{fi} = T_{0i} \exp(-m_i) \text{ when } k_f = \exp n_i,$$

$$c_i = m_i \exp(-n_i/D), \tag{22}$$

where m_i and n_i can be considered “free” parameters to help tune ASA for specific problems.

It has proven fruitful to use the same type of annealing schedule for the acceptance function h as used for the generating function g, but with the number of acceptance points, instead of the number of generated points, used to determine the k for the acceptance temperature.

New parameters α^i_{k+1} are generated from old parameters α^i_k from

$$\alpha^i_{k+1} = \alpha^i_k + y^i(B_i - A_i), \tag{23}$$

constrained by

$$\alpha^i_{k+1} \in [A_i, B_i]. \tag{24}$$

I.e., y^i’s are generated until a set of D are obtained satisfying these constraints.

2.1.5 Quenching

Another adaptive feature of ASA is its ability to perform quenching. This is applied by noting that the temperature schedule above can be redefined as

$$T_i(k_i) = T_{0i} \exp(-c_i k_i^{Q_i/D}),$$

$$c_i = m_i \exp(-n_i Q_i/D), \tag{25}$$

in terms of the “quenching factor” Q_i. The above proof fails if $Q_i > 1$ as

$$\sum_k \prod^D 1/k^{Q_i/D} = \sum_k 1/k^{Q_i} < \infty. \tag{26}$$

This simple calculation shows how the “curse of dimensionality” arises, and also gives a possible way of living with this disease. In ASA, the influence of large dimensions becomes clearly focused on the exponential of the power of k being $1/D$, as the annealing required to properly sample the space becomes prohibitively slow. So, if resources cannot commit to properly sample the space ergodically, then for some systems perhaps the next best procedure would be to turn on quenching, whereby Q_i can become on the order of the size of number of dimensions.

The scale of the power of $1/D$ temperature schedule used for the acceptance function can be altered in a similar fashion. However, this does not affect the annealing proof of ASA, and so this may be used without damaging the (weak) ergodicity property.

Many researchers have found it very attractive to take advantage of the ease of coding and implementing SA, utilizing its ability to handle quite complex cost functions and constraints. However,

doi:10.20944/preprints202009.0385.v2

the long time of execution of standard Boltzmann-type SA has many times driven these projects to utilize a temperature schedule too fast to satisfy the sufficiency conditions required to establish a true (weak) ergodic search. A logarithmic temperature schedule is consistent with the Boltzmann algorithm, e.g., the temperature schedule is taken to be

$$T_k = T_0 \frac{\ln k_0}{\ln k}, \tag{27}$$

where T is the "temperature," k is the "time" index of annealing, and k_0 is some starting index. This can be written for large k as

$$\Delta T = -T_0 \frac{\ln k_0 \Delta k}{k(\ln k)^2}, k \gg 1$$

$$T_{k+1} = T_k - T_0 \frac{\ln k_0}{k(\ln k)^2}. \tag{28}$$

However, some researchers using the Boltzmann algorithm use an exponential schedule, e.g.,

$$T_{k+1} = cT_k, 0 < c < 1$$

$$\frac{\Delta T}{T_k} = (c-1)\Delta k, k \gg 1$$

$$T_k = T_0 \exp\big((c-1)k\big), \tag{29}$$

with expediency the only reason given. The question arises, what is the value of this clear misuse of the claim to use SA to help solve these problems/systems? Adaptive simulated annealing (ASA) (Ingber, 1989a, 1993a), in fact does justify an exponential annealing schedule, but only if a particular distribution is used for the generating function.

In many cases it is clear that the researchers already know quite a bit about their system, and the convenience of the SA algorithm, together with the need for some global search over local optima, makes a strong practical case for the use of simulated quenching (SQ). In some of these cases, the researchers have been more diligent with regard to their numerical SQ work, and have compared the efficiency of SQ to some other methods they have tried. Of course, the point must be made that while SA's true strength lies in its ability to statistically deliver a true global optimum, there are no theoretical reasons for assuming it can be more efficient than any other algorithm that also can find this global optimum. E.g., Newton's algorithm is likely the best code for parabolic cost functions.

2.1.6 Generating probability density function

In a D-dimensional parameter space with parameters p^i having ranges $[A_i, B_i]$, about the k'th last saved point (e.g., a local optima), p^i_k, a new point is generated using a distribution defined by the product of distributions for each parameter, $g^i(y^i; T_i)$ in terms of random variables $y^i \in [-1, 1]$, where $p^i_{k+1} = p^i_k + y^i(B_i - A_i)$, and "temperatures" T_i,

$$g^i(y^i; T_i) = \frac{1}{2(|y^i| + T_i)\ln(1 + 1/T_i)}. \tag{30}$$

The OPTIONS USER_GENERATING_FUNCTION permits using an alternative to this ASA distribution function.

Preprints (www.preprints.org) | NOT PEER-REVIEWED | Posted: 8 October 2020 doi:10.20944/preprints202009.0385.v2

2.1.7 Acceptance probability density function

The cost functions, $C(p_{k+1}) - C(p_k)$, are compared using a uniform random generator, $U \in [0, 1)$, in a "Boltzmann" test: If

$$\exp[-\big(C(p_{k+1}) - C(p_k)\big)/T_{\text{cost}}] > U, \tag{31}$$

where T_{cost} is the "temperature" used for this test, then the new point is accepted as the new saved point for the next iteration. Otherwise, the last saved point is retained. The OPTIONS USER_ACCEPT_ASYMP_EXP or USER_ACCEPT_THRESHOLD permit using alternatives to this Boltzmann distribution function.

3 PATHINT/PATHTREE and qPATHINT/qPATHTREE

A paper discusses qPATHINT/qPATHTREE in more detail (Ingber, 2018a).

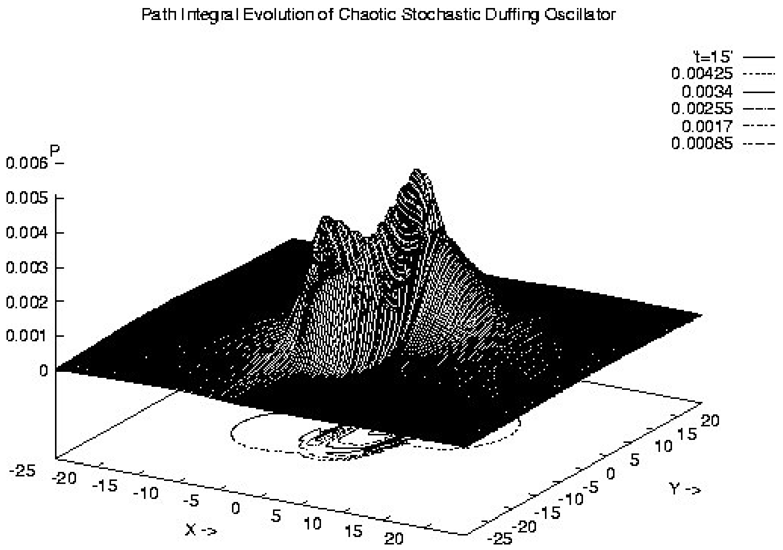

Fig. 2. This figure illustrates the evolution of the phase space for the purported model of chaos for the chaotic parameter $\omega_0 = 0.1$ during a transient period between $t = 12$ and $t = 15.5$, where foldings of the distribution were taken each $dt = 0.1$ interval. The non-chaos case with $\omega_0 = 1.0$ is similar in appearance except for the settling of transients. There is no evidence of chaos (Ingber *et al.*, 1996).

3.1 Path integral in Stratonovich (midpoint) representation

The path integral in the Feynman (midpoint) representation is used to examine discretization issues in time-dependent nonlinear systems (Langouche *et al.*, 1979, 1982; Schulman, 1981). (N.b. $g^\dagger$ in DM implies a prepoint evaluation.)

Unless explicitly stated, the Einstein summation convention is used which implies repeated indices signify summation; bars $|\ldots|$ imply no summation.

$$P[M_t|M_{t_0}]dM(t) = \int \ldots \int DM \exp\left(-\min \int_{t_0}^{t} dt' L\right) \delta\big(M(t_0) = M_0\big)\delta\big(M(t) = M_t\big)$$

$$DM = \lim_{u\to\infty} \prod_{\rho=1}^{u+1} g^{\dagger 1/2} \prod_G (2\pi\theta)^{-1/2} dM_\rho^G$$

$$L(\dot{M}^G, M^G, t) = \frac{1}{2}(\dot{M}^G - h^G) g_{GG'} (\dot{M}^{G'} - h^{G'}) + \frac{1}{2} h^G_{;G} + R/6 - V$$

$$\dot{M}^G(t) \to M^G_{\rho+1} - M^G_\rho, M^G(t) \to \frac{1}{2}(M^G_{\rho+1} + M^G_\rho), [\ldots]_{,G} = \frac{\partial[\ldots]}{\partial M^G}$$

$$h^G = g^G - \frac{1}{2} g^{-1/2} (g^{1/2} g^{GG'})_{,G'}, h^G_{;G} = h^G_{,G} + \Gamma^F_{GF} h^G = g^{-1/2} (g^{1/2} h^G)_{,G}$$

$$g_{GG'} = (g^{GG'})^{-1}, g = \det(g_{GG'})$$

$$\Gamma^F_{JK} \equiv g^{LF}[JK, L] = g^{LF}(g_{JL,K} + g_{KL,J} - g_{JK,L})$$

$$R = g^{JL}R_{JL} = g^{JL}g^{JK}R_{FJKL}$$

$$R_{FJKL} = \frac{1}{2}(g_{FK,JL} - g_{JK,FL} - g_{FL,JK} + g_{JL,FK}) + g_{MN}(\Gamma^M_{FK}\Gamma^N_{JL} - \Gamma^M_{FL}\Gamma^N_{JK}) \tag{32}$$

Non-constant diffusions add terms to drifts, and a Riemannian-curvature potential $R/6$ is induced for dimension > 1 in the Stratonovich/Feynman discretization.

3.2 Path integral in Ito (prepoint) representation

In the Ito (prepoint) representation:

$$P[M_t|M_{t_0}]dM(t) = \int \ldots \int DM \exp\big(- \min \int_{t_0}^{t} dt' L\big)\delta\big(M(t_0) = M_0\big)\delta\big(M(t) = M_t\big)$$

$$DM = \lim_{u\to\infty} \prod_{\rho=1}^{u+1} g^{1/2} \prod_G (2\pi\Delta t)^{-1/2} dM^G_\rho$$

$$L(\dot{M}^G, M^G, t) = \frac{1}{2}(\dot{M}^G - g^G)g_{GG'}(\dot{M}^{G'} - g^{G'}) + R/6$$

$$\dot{M}^G(t) \to M^G_{\rho+1} - M^G_\rho, M^G(t) \to M^G_\rho$$

$$(g_{GG'}) = (g^{GG'})^{-1}, g = \det(g_{GG'}) \tag{33}$$

Here the diagonal diffusions are $g^{|GG|}$ and the drifts are g^G.

3.3 Path-integral Riemannian geometry

The midpoint derivation derives a Riemannian geometry with metric defined by the inverse of the covariance matrix

$$g_{GG'} = (g^{GG'})^{-1} \tag{34}$$

and where R is the Riemannian curvature

$$R = g^{JL}R_{JL} = g^{JL}g^{JK}R_{FJKL} \tag{35}$$

An Ito prepoint discretization for the same probability distribution P gives a simpler algebraic form,

$$M(\bar{t}_s) = M(t_s)$$

$$L = \frac{1}{2}(dM^G/dt - g^G)g_{GG'}(dM^{G'}/dt - g^{G'}) - V \tag{36}$$

but the Lagrangian L so specified does not satisfy a variational principle useful for moderate to large noise. Its variational principle is only useful in the weak-noise limit. This often means that finer meshes are required.

3.4 Three approaches are mathematically equivalent

Three basic different approaches are mathematically equivalent:

(a) Fokker-Planck/Chapman-Kolmogorov partial-differential equations
(b) Langevin coupled stochastic-differential equations
(c) Lagrangian or Hamiltonian path-integrals

All three are described here as many researchers are familiar with at least one of these approaches to complex systems.

The path-integral approach is useful to define intuitive physical variables from the Lagrangian L in terms of underlying variables M^G:

$$\text{Momentum}: \ \Pi^G = \frac{\partial L}{\partial(\partial M^G/\partial t)}$$

$$\text{Mass}: \ g_{GG'} = \frac{\partial L}{\partial(\partial M^G/\partial t)\partial(\partial M^{G'}/\partial t)}$$

$$\text{Force}: \ \frac{\partial L}{\partial M^G}$$

$$F = ma: \ \delta L = 0 = \frac{\partial L}{\partial M^G} - \frac{\partial}{\partial t}\frac{\partial L}{\partial(\partial M^G/\partial t)} \tag{37}$$

The Momenta $= \Pi^G$ are often called canonical momenta. They have been used as Canonical Momenta Indicators (CMI) for all the disciplines described in this paper, and are proposed to be used in the application to COVID-19 forecasting.

Differentiation especially of noisy systems often introduces more noise. The path-integral often gives superior numerical performance because integration is a smoothing process.

3.4.1 Stochastic differential equation (SDE)

The Stratonovich (midpoint discretized) Langevin equations can be analyzed in terms of the Wiener process dW^i. This can be developed with Gaussian noise $\eta^i = dW^i/dt$, with some care taken in the limit of small dt.

$$dM^G = f^G\big(t, M(t)\big)dt + \hat{g}_i^G\big(t, M(t)\big)dW^i$$

$$\dot{M}^G(t) = f^G\big(t, M(t)\big) + \hat{g}_i^G\big(t, M(t)\big)\eta^i(t)$$

$$dW^i \to \eta^i dt$$

$$M = \{M^G; G = 1, \ldots, \Lambda\}$$

$$\eta = \{\eta^i; i = 1, \ldots, N\}$$

$$\dot{M}^G = dM^G/dt$$

$$< \eta^j(t) >_\eta = 0, < \eta^j(t), \eta^{j'}(t') >_\eta = \delta^{jj'}\delta(t - t') \tag{38}$$

η^i represents Gaussian white noise.

3.4.2 Partial differential equation (PDE)

The Fokker-Planck, sometimes defined as Chapman-Kolmogorov, partial differential equation is:

$$P_{,t} = \frac{1}{2}(g^{GG'}P)_{,GG'} - (g^G P)_{,G} + VP$$

$$P = < P_\eta >_\eta$$

$$g^G = f^G + \frac{1}{2}\hat{g}_i^{G'}\hat{g}_{i,G'}^G$$

$$g^{GG'} = \hat{g}_i^G \hat{g}_i^{G'}$$

$$(\ldots)_{,G} = \partial(\ldots)/\partial M^G \tag{39}$$

g^G replaces f^G in the SDE if the Ito (prepoint discretized) calculus is used. If boundary conditions are added as Lagrange multipliers, these enter as a "potential" V creating a Schrodinger-type equation.

3.5 PATHINT/qPATHINT code

qPATHINT is an N-dimensional code developed to calculate the propagation of quantum variables in the presence of shocks. Many real systems propagate in the presence of sudden changes of state dependent on time. qPATHINT is based on the classical-physics code, PATHINT, which has been useful in several systems across several disciplines. Applications have been made to Statistical Mechanics of Neocortical Interactions (SMNI) and Statistical Mechanics of Financial Markets (SMFM) (Ingber, 2017a,b,c).

To numerically calculate the path integral for serial changes in time, standard Monte Carlo techniques generally are not useful. PATHINT was originally developed for this purpose. The PATHINT C code of about 7500 lines of code using the GCC C-compiler was rewritten to use double complex variables instead of double variables, and further developed for arbitrary N dimensions, creating qPATHINT. The outline of the code is described here for classical or quantum systems, using generic coordinates q (Ingber, 2016a, 2017a,b).

The distribution (probabilities for classical systems, wave-functions for quantum systems) can be numerically approximated to a high degree of accuracy using a histogram procedure, developing sums of rectangles of height P_i and width Δq^i at points q^i.

3.6 Shocks

Many real-world systems propagate in the presence of continual "shocks". [q]PATHINT and [q]PATHTREE (a fast binominal code based on PATHINT) have demonstrated that these issues present no problems in applying these algorithms.

In SMNI, collisions occur via regenerative Ca^{2+} waves. There also are interactions with the changing magnetic vector potential $\mathbf{A}$ due to highly synchronous neuronal firings.

In SMFM applications, shocks occur due to future dividends, changes in interest rates, changes in asset distributions, etc.

3.7 PATHINT/qPATHINT histograms

A one-dimensional path-integral in variable q in the prepoint Ito discretization is developed in terms of the kernel/propagator G, for each of its intermediate integrals, as

$$P(q;t+\Delta t) = \int dq' [g^{1/2} (2\pi\Delta t)^{-1/2} \exp(-L\,\Delta t)] P(q';t) = \int dq' G(q,q';\Delta t) P(q';t)$$

$$P(q;t) = \sum_{i=1}^{N} \pi(q-q^i) P_i(t)$$

$$\pi(q-q^i) = 1\,,\ (q^i - \frac{1}{2}\Delta q^{i-1}) \le q \le (q^i + \frac{1}{2}\Delta q^i); 0\,,\ \text{otherwise} \tag{40}$$

This yields

$$P_i(t+\Delta t) = T_{ij}(\Delta t) P_j(t)$$

$$T_{ij}(\Delta t) = \frac{2}{\Delta q^{i-1} + \Delta q^i} \int\limits_{q^i - \Delta q^{i-1}/2}^{q^i + \Delta q^i/2} dq \int\limits_{q^j - \Delta q^{j-1}/2}^{q^j + \Delta q^j/2} dq' G(q,q';\Delta t) \tag{41}$$

T_{ij} is a banded matrix representing the Gaussian nature of the short-time probability centered about the drift.

Several projects have used this algorithm (Ingber & Nunez, 1995; Ingber *et al.*, 1996; Ingber & Wilson, 1999; Wehner & Wolfer, 1983a,b, 1987). Special 2-dimensional codes were developed for specific projects in Statistical Mechanics of Combat (SMC), SMNI and SMFM, e.g., to handle boundary conditions (Ingber, 2000; Ingber *et al.*, 1991a; Ingber & Nunez, 1995).

3.8 Meshes for [q]PATHINT

Explicit dependence of L on time t can be included. The mesh Δq^i is strongly dependent on diagonal elements of the diffusion matrix, e.g.,

$$\Delta q^i \approx (\Delta t g^{|ii|})^{1/2} \tag{42}$$

This constrains the dependence of the covariance of each variable to be a (nonlinear) function of that variable to present a rectangular underlying mesh. Since integration is inherently a smoothing process (Ingber, 1990), coarser meshes are used relative to the corresponding stochastic differential equation(s) (Wehner & Wolfer, 1983a).

By considering the contributions to the first and second moments, conditions on the time and variable meshes can be derived. Thus Δt can be measured by the diffusion divided by the square of the drift.

3.9 Lessons learned from SMFM and SMNI

SMNI qPATHINT has emphasized the requirement of broad-banded kernels for oscillatory quantum states.

SMFM PATHTREE, and its derived qPATHTREE, is a different options code, based on path-integral error analyses, permitting a new very fast binary calculation, also applied to nonlinear time-dependent systems (Ingber *et al.*, 2001). However, in contrast to the present PATHINT/qPATHINT code that has been generalized to N dimensions, currently an SMFM [q]PATHTREE is faster, but still only a binary tree with N = 1 and cannot be effectively applied to multivariate quantum oscillatory systems (Ingber, 2016a, 2017a,b).

4 Statistical Mechanics of Neocortical Interactions (SMNI)

A paper discusses SMNI in more detail (Ingber, 2018a).

This project calculates quantum Ca^{2+} interactions with EEG. EEG is synonymous with large-scale neocortical firings during attentional tasks as measured by large-amplitude electroencephalographic (EEG) recordings. Only very specific calcium ions, Ca^{2+}, are considered, those arising from regenerative calcium waves generated at tripartite neuron-astrocyte-neuron synapses. Indeed, it is important to note that Ca^{2+} ions, and specifically Ca^{2+} waves, influence many processes in the brain (Ross, 2012), but this study focuses on free waves generated at tripartite synapses (Lallouette *et al.*, 2019) because of their calculated direct interactions with large synchronous neuronal firings.

The theory and codes for ASA and [q]PATHINT have been well tested across many disciplines by multiple users.

The current project which includes quantum influences most certainly is speculative, but it is testable. As reported here, fitting such models to EEG tests some aspects of this project. This is a somewhat indirect path, but not novel to many physics paradigms that are tested by experiment or computation.

While SMNI has been developed since 1981, and been confirmed by many tests, this evolving model including ionic scales has been part of multiple papers relatively recently, since 2012. Classical physics calculations support these extended SMNI models and are consistent with experimental data. Quantum physics calculations also support these extended SMNI models and, while they too are consistent with experimental data, it is quite speculative that they can persist in neocortex. Admittedly, it is surprising that detailed calculations continue to support this model, and so it is worth continued examination it until it is theoretically or experimentally proven to be false.

SMNI has been developed since 1981, scaling aggregate synaptic interactions to neuronal firings, up to minicolumnar-macrocolumnar columns of neurons to mesocolumnar dynamics, up to columns of neuronal firings, up to regional macroscopic sites (Ingber, 1981, 1982, 1983, 1984a, 1985, 1994).

SMNI has calculated agreement/fits with experimental data from various aspects of neocortical interactions, e.g., properties of short-term memory (STM) (Ingber, 2012b), including its capacity (auditory 7±2 and visual 4±2) (Ericsson & Chase, 1982; Zhang & Simon, 1985), duration, stability, primacy versus recency rule, as well other phenomenon, e.g., Hick's law (Hick, 1952; Ingber, 1999; Jensen, 1987), interactions within macrocolumns calculating mental rotation of images, etc (Ingber, 1982, 1983, 1984a, 1985, 1994). SMNI scaled mesocolumns across neocortical regions to fit EEG data (Ingber, 1997a,b, 2012b).

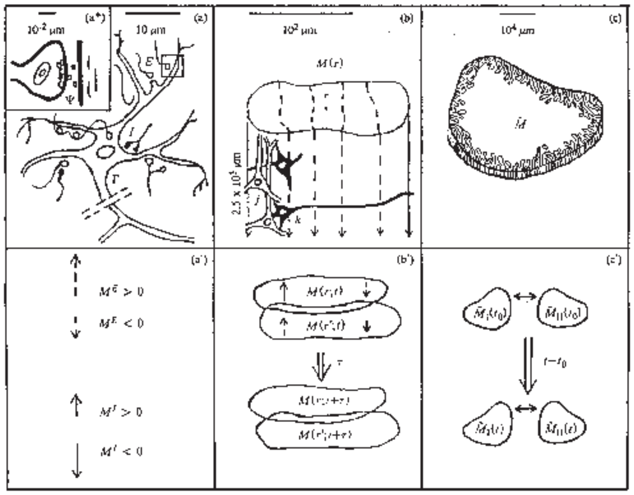

Fig. 3. Illustrated are three SMNI biophysical scales (Ingber, 1982, 1983): (a)-(a*)-(a') microscopic neurons; (b)-(b') mesocolumnar domains; (c)-(c') macroscopic regions.
(a*): synaptic inter-neuronal interactions, scaled up to mesocolumns, phenomenologically described by the mean and variance of a distribution Ψ
(a): intraneuronal transmissions phenomenologically described by the mean and variance of Γ
(a'): collective mesocolumnar-averaged inhibitory (I) and excitatory (E) neuronal firings M
(b): vertical organization of minicolumns including their horizontal layers, yielding a physiological entity, the mesocolumn
(b'): overlapping mesocolumns at locations r and r' from times t and $t+\tau$, τ on the order of 10 msec
(c): macroscopic regions of neocortex arising from many mesocolumnar domains
(c'): regions coupled by long-ranged interactions

4.1 Synaptic interactions

The short-time conditional probability distribution of firing of a given neuron firing given just-previous firings of other neurons is calculated from chemical and electrical intra-neuronal interactions (Ingber, 1982, 1983). Given its previous interactions with k neurons within τ_j of 5-10 msec, the conditional probability that neuron j fires ($\sigma_j = +1$) or does not fire ($\sigma_j = -1$) is

$$p_{\sigma_j} = \Gamma\Psi = \frac{\exp(-\sigma_j F_j)}{\exp(F_j) + \exp(-F_j)}$$

$$F_j = \frac{V_j - \sum\limits_k a^*_{jk} v_{jk}}{\left(\pi \sum\limits_{k'} a^*_{jk'}(v^2_{jk'} + \phi^2_{jk'})\right)^{1/2}}$$

$$a_{jk} = \frac{1}{2} A_{|jk|}(\sigma_k + 1) + B_{jk} \tag{43}$$

The contribution to polarization achieved at an axon given activity at a synapse, taking into account averaging over different neurons, geometries, etc., is given by Γ, the "intra-neuronal" probability distribution. Ψ is the "inter-neuronal" probability distribution, of thousands of quanta of neurotransmitters released at one neuron's presynaptic site effecting a (hyper-)polarization at another neuron's postsynaptic site, taking into account interactions with neuromodulators, etc. This development holds for Γ Poisson, and for Ψ Poisson or Gaussian.

V_j is the depolarization threshold in the somatic-axonal region. v_{jk} is the induced synaptic polarization of E or I type at the axon, and ϕ_{jk} is its variance. The efficacy a_{jk} is a sum of A_{jk} from the connectivity between neurons, activated if the impinging k-neuron fires, and B_{jk} from spontaneous background noise. The efficacy is related to the impedance across synaptic gaps.

4.2 Neuronal interactions

Aggregation up to the mesoscopic scale from the microscopic synaptic scale uses mesoscopic probability P

$$\begin{aligned} P &= \prod_G P^G[M^G(r;t+\tau)|M^{\bar{G}}(r';t)] \\ &= \sum_{\sigma_j} \delta\left(\sum_{jE} \sigma_j - M^E(r;t+\tau)\right) \delta\left(\sum_{jI} \sigma_j - M^I(r;t+\tau)\right) \prod_j^N p_{\sigma_j} \end{aligned} \tag{44}$$

M represents a mesoscopic scale of columns of N neurons, with subsets E and I, represented by p_{q_i}. The "delta"-functions δ-constraint represents an aggregate of many neurons in a column. G is used to represent excitatory (E) and inhibitory (I) contributions. $\bar{G}$ designates contributions from both E and I.

The path integral is derived in terms of mesoscopic Lagrangian L. The short-time distribution of firings in a minicolumn, given its just previous interactions with all other neurons in its macrocolumn, is thereby defined.

4.3 Columnar interactions

In the prepoint (Ito) representation the SMNI Lagrangian L is

$$L = \sum_{G,G'} (2N)^{-1}(\dot{M}^G - g^G) g_{GG'} (\dot{M}^{G'} - g^{G'})/(2N\tau) - V'$$

$$g^G = -\tau^{-1}(M^G + N^G \tanh F^G)$$

$$g^{GG'} = (g_{GG'})^{-1} = \delta_G^{G'} \tau^{-1} N^G \operatorname{sech}^2 F^G$$

$$g = \det(g_{GG'}) \tag{45}$$

The threshold factor F^G is derived as

$$F^G = \sum_{G'} \frac{\nu^G + \nu^{\ddagger E'}}{\left((\pi/2)[(v_{G'}^G)^2 + (\phi_{G'}^G)^2](\delta^G + \delta^{\ddagger E'})\right)^{1/2}}$$

$$\nu^G = V^G - a_{G'}^G v_{G'}^G N^{G'} - \frac{1}{2} A_{G'}^G v_{G'}^G M^{G'}, \nu^{\ddagger E'} = -a_{E'}^{\ddagger E} v_{E'}^E N^{\ddagger E'} - \frac{1}{2} A_{E'}^{\ddagger E} v_{E'}^E M^{\ddagger E'}$$

$$\delta^G = a_{G'}^G N^{G'} + \frac{1}{2} A_{G'}^G M^{G'}, \delta^{\ddagger E'} = a_{E'}^{\ddagger E} N^{\ddagger E'} + \frac{1}{2} A_{E'}^{\ddagger E} M^{\ddagger E'}$$

$$a^G_{G'} = \frac{1}{2} A^G_{G'} + B^G_{G'}, a^{\ddagger E}_{E'} = \frac{1}{2} A^{\ddagger E}_{E'} + B^{\ddagger E}_{E'} \tag{46}$$

where $A^G_{G'}$ is the columnar-averaged direct synaptic efficacy, $B^G_{G'}$ is the columnar-averaged background-noise contribution to synaptic efficacy. The "‡" parameters arise from regional interactions across many macrocolumns.

4.4 SMNI parameters from experiments

All values of parameters and their bounds are taken from experimental data, not arbitrarily fit to specific phenomena.

$N^G = \{N^E = 160,\ N^I = 60\}$ was set for for visual neocortex, $\{N^E = 80,\ N^I = 30\}$ was set for all other neocortical regions, $M^{G'}$ and $N^{G'}$ in F^G are afferent macrocolumnar firings scaled to efferent minicolumnar firings by $N/N^* \approx 10^{-3}$. N^* is the number of neurons in a macrocolumn, about 10^5. V' includes nearest-neighbor mesocolumnar interactions. τ is usually considered to be on the order of 5-10 ms.

Other values also are consistent with experimental data, e.g., $V^G = 10$ mV, $v^G_{G'} = 0.1$ mV, $\phi^G_{G'} = 0.03^{1/2}$ mV.

Nearest-neighbor interactions among columns give dispersion relations that were used to calculate speeds of mental visual rotation (Ingber, 1982, 1983).

The phenomenological wave equation cited by EEG theorists, permitting fits of SMNI to EEG data (Ingber, 1995), was derived using the variational principle applied to the SMNI Lagrangian.

This creates an audit trail from synaptic parameters to the statistically averaged regional Lagrangian.

4.5 Verification of basic SMNI hypothesis

The core SMNI hypothesis first developed circa 1980 (Ingber, 1981, 1982, 1983) is that highly synchronous patterns of neuronal firings in fact process high-level information. Only since 2012 has this hypothesis been verified experimentally (Asher, 2012; Salazar *et al.*, 2012).

4.6 Comparing EEG testing data with training data

Using EEG data from http://physionet.nlm.nih.gov/pn4/erpbci (Citi *et al.*, 2010; Goldberger *et al.*, 2000), SMNI was fit to highly synchronous waves (P300) during attentional tasks, for each of 12 subjects, it was possible to find 10 Training runs and 10 Testing runs (Ingber, 2016b).

Spline-Laplacian transformations on the EEG potential Φ are proportional to the SMNI M^G firing variables at each electrode site. The electric potential Φ is experimentally measured by EEG, not $\mathbf{A}$, but both are due to the same currents $\mathbf{I}$. Therefore, $\mathbf{A}$ is linearly proportional to Φ with a simple scaling factor included as a parameter in fits to data. Additional parameterization of background synaptic parameters, $B^G_{G'}$ and $B^{\ddagger E}_{E'}$, modify previous work.

The $\mathbf{A}$ model outperformed the no-$\mathbf{A}$ model, where the no-$\mathbf{A}$ model simply has used $\mathbf{A}$-non-dependent synaptic parameters. Cost functions with an $|\mathbf{A}|$ model were much worse than either the $\mathbf{A}$ model or the no-$\mathbf{A}$ model. Runs with different signs on the drift and on the absolute value of the drift also gave much higher cost functions than the $\mathbf{A}$ model.

doi:10.20944/preprints202009.0385.v2

4.7 PATHINT STM

The evolution of a Balanced Centered model (BC) after 500 foldings of $\Delta t = 0.01$, 5 unit of relaxation time τ, exhibits the existence of ten well developed peaks. These peaks are identified with possible trappings of firing patterns.

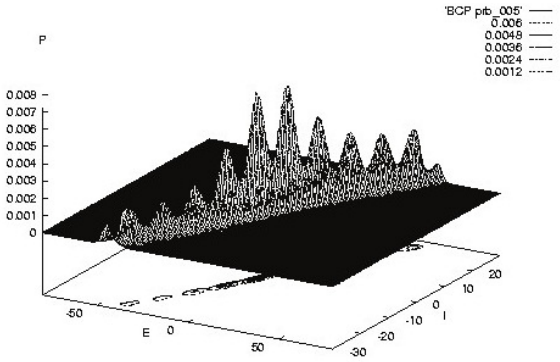

Fig 4. Illustrated is SMNI STM Model BC at the evolution at 5τ (Ingber & Nunez, 1995).

This describes the "7 ± 2" rule, as calculated by SMNI PATHINT (Ingber & Nunez, 1995).

4.8 PATHINT STM visual

The evolution of a Balanced Centered Visual model (BCV), with double the number of neurons/minicolumn than other neocortical regions, after 1000 foldings of $\Delta t = 0.01$, 10 unit of relaxation time τ, exhibits the existence of four well developed peaks. These peaks are identified with possible trappings of firing patterns. Other peaks at lower scales are clearly present, numbering on the same order as in the BC' model, as the strength in the original peaks dissipates throughout firing space, but these are much smaller and therefore much less probable to be accessed.

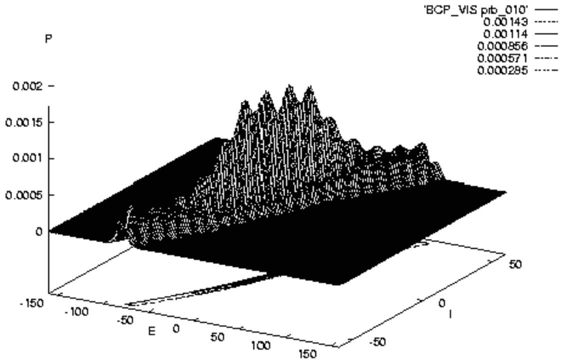

Fig. 5. Illustrates is SMNI STM Model BCV at the evolution at 10τ (Ingber & Nunez, 1995).

This describes the "4 ± 2" rule for visual STM (Ingber & Nunez, 1995).

4.9 Tripartite synaptic interactions

The human brain contains over 10^{11} cells, about half of which are neurons. The other half are glial cells. Astrocytes comprise a good fraction of glial cells, possibly the majority. Many papers examine the influence of astrocytes on synaptic processes (Agulhon *et al.*, 2008; Araque & Navarrete, 2010; Banaclocha *et al.*, 2010; Bellinger, 2005; Innocenti *et al.*, 2000; Pereira & Furlan, 2009; Reyes & Parpura, 2009; Scemes & Giaume, 2006; Volterra *et al.*, 2014).

http://www.astrocyte.info claims they are the most numerous cells in the human brain. Unlike the previous ideology of astrocytes being "filler" cells, they are very active in the central nervous system and greatly outnumber neurons,

Glutamate release from astrocytes through a Ca^{2+}-dependent mechanism can activate receptors at the presynaptic terminals. Intercellular calcium waves (ICWs) may travel over hundreds of astrocytes propagating over many neuronal synapses. ICWs contribute to control synaptic activity. Glutamate is released in a regenerative manner, with subsequent cells that are involved in the calcium wave releasing additional glutamate (Ross, 2012).

$[Ca^{2+}]$ (concentrations of Ca^{2+}) affect increased release probabilities at synaptic sites, by enhancing the release of gliotransmitters. (Free Ca^{2+} waves are considered here, not intracellular astrocyte calcium waves in situ which also increase neuronal firings.)

These free regenerative Ca^{2+} waves, arising from astrocyte-neuron interactions, couple to the magnetic vector potential **A** produced by highly synchronous collective firings, e.g., during selective attention tasks, as measured by EEG.

4.9.1 Canonical momentum $\mathbf{\Pi} = \mathbf{p} + q\mathbf{A}$

As derived in the Feynman (midpoint) representation of the path integral, the canonical momentum, $\mathbf{\Pi}$, defines the dynamics of a moving particle with momentum $\mathbf{p}$ in an electromagnetic field. In SI units,

$$\mathbf{\Pi} = \mathbf{p} + q\mathbf{A} \tag{47}$$

where $q = -2e$ for Ca^{2+}, e is the magnitude of the charge of an electron $= 1.6 \times 10^{-19}$ C (Coulomb), and $\mathbf{A}$ is the electromagnetic vector potential. (In Gaussian units $\mathbf{\Pi} = \mathbf{p} + q\mathbf{A}/c$, where c is the speed of light.) $\mathbf{A}$ represents three components of a 4-vector.

4.9.2 Vector potential of wire

A columnar firing state is modeled as a wire/neuron with current $\mathbf{I}$ measured in A = Amperes = C/s,

$$\mathbf{A}(t) = \frac{\mu}{4\pi} \int \frac{dr}{r} \mathbf{I} \tag{48}$$

along a length z observed from a perpendicular distance r from a line of thickness r_0. If far-field retardation effects are neglected, this yields

$$\mathbf{A} = \frac{\mu}{4\pi} \mathbf{I} \log\left(\frac{r}{r_0}\right) \tag{49}$$

where μ is the magnetic permeability in vacuum $= 4\pi 10^{-7}$ H/m (Henry/meter). Note the insensitive log dependence on distance.

The contribution to $\mathbf{A}$ includes minicolumnar lines of current from hundreds to thousands of macrocolumns, within a region not so large to include many convolutions, but still contributing to large synchronous bursts of EEG.

Electric $\mathbf{E}$ and magnetic $\mathbf{B}$ fields, derivatives of $\mathbf{A}$ with respect to r, do not possess this logarithmic insensitivity to distance, and therefore they do not linearly accumulate strength within and across macrocolumns.

Estimates of contributions from synchronous firings to P300 measured on the scalp are tens of thousands of macrocolumns spanning 100 to 100's of cm^2. Electric fields generated from a minicolumn may fall by half within 5-10 mm, the range of several macrocolumns.

There are other possible sources of magnetic vector potentials not described as wires with currents (Majhi & Ghosh, 2018). Their net effects plausibly would be included the vector magnetic potential of net synchronous firings, but not their functional forms as derived here.

4.9.3 Effects of vector potential on momenta

The momentum $\mathbf{p}$ for a Ca^{2+} ion with mass $m = 6.6 \times 10^{-26}$ kg, speed on the order of 50 μm/s to 100 μm/s, is on the order of 10^{-30} kg-m/s. Molar concentrations of Ca^{2+} waves, comprised of tens of thousands of free ions representing about 1% of a released set, most being buffered, are within a range of about 100 μm to as much as 250 μm, with a duration of more than 500 ms, and with [Ca^{2+}] ranging from 0.1-5 μM (μM $= 10^{-3}$ mol/m^3).

The magnitude of the current is taken from experimental data on dipole moments $\mathbf{Q} = |\mathbf{I}|\hat{\mathbf{z}}$ where $\hat{\mathbf{z}}$ is the direction of the current $\mathbf{I}$ with the dipole spread over z. $\mathbf{Q}$ ranges from 1 pA-m $= 10^{-12}$ A-m for a pyramidal neuron (Murakami & Okada, 2006), to 10^{-9} A-m for larger neocortical mass (Nunez & Srinivasan, 2006). These currents give rise to $q\mathbf{A} \approx 10^{-28}$ kg-m/s. The velocity of a Ca^{2+} wave can be ≈20-50 μm/s. In neocortex, a typical Ca^{2+} wave of 1000 ions, with total mass $m = 6.655 \times 10^{-23}$ kg times a speed of ≈20-50 μm/s, gives $\mathbf{p} \approx 10^{-27}$ kg-m/s.

Taking 10^4 synchronous firings in a macrocolumn, leads to a dipole moment $|\mathbf{Q}| = 10^{-8}$ A-m. Taking z to be $10^2 \mu$m $= 10^{-4}$ m, a couple of neocortical layers, gives $|q\mathbf{A}| \approx 2 \times 10^{-19} \times 10^{-7} \times 10^{-8}/10^{-4} = 10^{-28}$ kg-m/s,

4.9.4 Results including quantum scales

The wave function ψ_e describing the interaction of $\mathbf{A}$ with $\mathbf{p}$ of Ca^{2+} wave packets was derived in closed form from the Feynman representation of the path integral using path-integral techniques (Schulten, 1999), modified here to include $\mathbf{A}$.

$$\psi_{\rm e}(t) = \int d\mathbf{r}_0 \psi_0 \psi_F = \left[\frac{1 - i\hbar t/(m\Delta\mathbf{r}^2)}{1 + i\hbar t/(m\Delta\mathbf{r}^2)} \right]^{1/4} \left[\pi\Delta\mathbf{r}^2 \{1 + [\hbar t/(m\Delta\mathbf{r}^2)]^2\} \right]^{-1/4}$$

$$\times \exp\left[-\frac{[\mathbf{r} - (\mathbf{p}_0 + q\mathbf{A})t/m]^2}{2\Delta\mathbf{r}^2} \frac{1 - i\hbar t/(m\Delta\mathbf{r}^2)}{1 + [\hbar t/(m\Delta\mathbf{r}^2)]^2} + i\frac{\mathbf{p}_0 \cdot \mathbf{r}}{\hbar} - i\frac{(\mathbf{p}_0 + q\mathbf{A})^2 t}{2\hbar m} \right]$$

$$\psi_F(t) = \int \frac{d\mathbf{p}}{2\pi\hbar} \exp\left[\frac{i}{\hbar} \left(\mathbf{p}(\mathbf{r} - \mathbf{r}_0) - \frac{\mathbf{\Pi}^2 t}{(2m)} \right) \right] = \left[\frac{m}{2\pi i\hbar t} \right]^{1/2} \exp\left[\frac{im(\mathbf{r} - \mathbf{r}_0 - q\mathbf{A}t/m)^2}{2\hbar t} - \frac{i(q\mathbf{A})^2 t}{2m\hbar} \right]$$

$$\psi_0 = \psi(\mathbf{r}_0, t = 0) = \left(\frac{1}{\pi\Delta\mathbf{r}^2} \right)^{1/4} \exp\left(-\frac{\mathbf{r}_0^2}{2\Delta\mathbf{r}^2} + i\frac{\mathbf{p}_0 \cdot \mathbf{r}_0}{\hbar} \right) \tag{50}$$

where ψ_0 is the initial Gaussian packet, ψ_F is the free-wave evolution operator, $\hbar$ is the Planck constant, q is the electronic charge of Ca^{2+} ions, m is the mass of a wave-packet of 1000 Ca^{2+} ions, $\Delta\mathbf{r}^2$ is the spatial variance of the wave-packet, the initial momentum is $\mathbf{p}_0$, and the evolving canonical momentum is $\mathbf{\Pi} = \mathbf{p} + q\mathbf{A}$. Detailed calculations show that $\mathbf{p}$ of the Ca^{2+} wave packet and $q\mathbf{A}$ of the EEG field make about equal contributions to $\mathbf{\Pi}$ (Ingber, 2015a).

4.9.5 SMNI + Ca^{2+} wave-packet

Tripartite influence on synaptic $B^G_{G'}$ is measured by the ratio of packet's $< \mathbf{p}(t) >_{\psi*\psi}$ to $< \mathbf{p}_0(t_0) >_{\psi*\psi}$ at the onset of each attentional task. Here $<>_{\psi*\psi}$ is taken over $\psi^*_{\rm e}\, \psi_{\rm e}$.

$$< \mathbf{p} >_{\psi*\psi} = m\frac{< \mathbf{r} >_{\psi*\psi}}{t - t_0} = \frac{q\mathbf{A} + \mathbf{p}_0}{m^{1/2}|\Delta\mathbf{r}|} \left(\frac{(\hbar t)^2 + (m\Delta\mathbf{r}^2)^2}{\hbar t + m\Delta\mathbf{r}^2} \right)^{1/2} \tag{51}$$

$\mathbf{A}$ changes slower than $\mathbf{p}$, so static approximation of $\mathbf{A}$ used to derive $\psi_{\rm e}$ and $< \mathbf{p} >_{\psi*\psi}$ is reasonable to use within P300 EEG epochs, resetting $t = 0$ at the onset of each classical EEG measurement (1.953 ms apart), using the current $\mathbf{A}$. This permits tests of interactions across scales in a classical context. Note the explicit dependence on $\hbar$, permitting testing quantum sensitivity.

4.9.6 Results using $< \mathbf{p} >_{\psi*\psi}$

$< \mathbf{p} >_{\psi*\psi}$ was used in classical-physics SMNI fits to EEG data using ASA. Runs using 1M or 100K generated states gave results not much different. Training with ASA used 100K generated states over 12 subjects with and without $\mathbf{A}$, followed by 1000 generated states with the simplex local code contained with ASA. Training and Testing runs on XSEDE.org for this project has taken an equivalent of several months of CPU on the XSEDE.org UCSD platform Comet. These calculations use one additional parameter across all EEG regions to weight the contribution to synaptic background $B^G_{G'}$. $\mathbf{A}$ is taken to be proportional to the currents measured by EEG, i.e., firings M^G. Otherwise, the "zero-fit-parameter" SMNI philosophy was enforced, wherein parameters are picked from experimentally determined values or within experimentally determined ranges (Ingber, 1984a).

4.9.7 Quantum Zeno effects

The quantum-mechanical wave function of the wave packet was shown to "survive" overlaps after multiple collisions, due to their regenerative processes during the observed long durations of hundreds of ms. Thus, Ca^{2+} waves may support a Zeno or "bang-bang" effect which may promote long coherence times (Burgarth *et al.*, 2018; Facchi *et al.*, 2004; Facchi & Pascazio, 2008; Giacosa & Pagliara, 2014; Kozlowski *et al.*, 2015; Muller *et al.*, 2016; Patil *et al.*, 2015; Wu *et al.*, 2012).

Of course, the Zeno/"bang-bang" effect may exist only in special contexts, since decoherence among particles is known to be very fast, e.g., faster than phase-damping of macroscopic classical particles colliding with quantum particles (Preskill, 2015).

The wave may be perpetuated by the constant collisions of ions as they enter and leave the wave packet due to the regenerative collisions by the Zeno/"bang-bang" effect. qPATHINT can calculate the coherence stability of the wave due to serial shocks.

4.9.8 Survival of wave packet

In momentum space, the wave packet $\phi(\mathbf{p}, t)$ is considered as being "kicked" from $\mathbf{p}$ to $\mathbf{p} + \delta\mathbf{p}$. Assume that random repeated kicks of $\delta\mathbf{p}$ result in $< \delta\mathbf{p} >\approx 0$, and that each kick keeps the variance $\Delta(\mathbf{p}+\delta\mathbf{p})^2 \approx \Delta(\mathbf{p})^2$. Then, the overlap integral at the moment t of a typical kick between the new and old state is

$$\begin{aligned}
< \phi^*(\mathbf{p}+\delta\mathbf{p}, t)|\phi(\mathbf{p}, t) > &= \exp\left(\frac{i\kappa + \rho}{\sigma}\right) \\
\kappa &= 8\,\delta\mathbf{p}\,\Delta\mathbf{p}^2\,\hbar m(q\mathbf{A} + \mathbf{p}_0)t - 4(\delta\mathbf{p}\Delta\mathbf{p}^2 t)^2 \\
\rho &= -(\delta\mathbf{p}\,\hbar m)^2 \\
\sigma &= 8(\Delta\mathbf{p}\,\hbar m)^2
\end{aligned} \tag{52}$$

where $\phi(\mathbf{p} + \delta\mathbf{p}, t)$ is the normalized wave function in $\mathbf{p} + \delta\mathbf{p}$ momentum space. A crude estimate is obtained of the survival time amplitude $A(t)$ and survival probability $p(t)$ (Facchi & Pascazio, 2008),

$$\begin{aligned}
A(t) &=< \phi^*(\mathbf{p}+\delta\mathbf{p}, t)|\phi(\mathbf{p}, t) > \\
p(t) &= |A(t)|^2
\end{aligned} \tag{53}$$

These numbers yield:

$$< \phi^*(\mathbf{p}+\delta\mathbf{p}, t)|\phi(\mathbf{p}, t) >= \exp\left(i(1.67 \times 10^{-1}t - 1.15 \times 10^{-2}t^2) - 1.25 \times 10^{-7}\right) \tag{54}$$

Even many small repeated kicks do not appreciably affect the real part of ϕ, and these projections do not appreciably destroy the original wave packet, giving a survival probability per kick as $p(t) \approx \exp(-2.5 \times 10^{-7}) \approx 1 - 2.5 \times 10^{-7}$.

The time-dependent phase terms are sensitive to times of tenths of a sec. These times are prominent in STM and in synchronous neural firings. Therefore, $\mathbf{A}$ effects on Ca^{2+} wave functions may maximize their influence on STM at frequencies consistent with synchronous EEG during STM.

All these calculations support this model, in contrast to other models of quantum brain processes without such specific calculations and support (Hagan *et al.*, 2002; Hameroff & Penrose, 2013; McKemmish *et al.*, 2009).

4.10 Nano-robotic applications

There is the possibility of carrying pharmaceutical products in nanosystems that could affect unbuffered Ca^{2+} waves in neocortex (Ingber, 2015a). A Ca^{2+}-wave momentum-sensor could act like a piezoelectric device.

At the onset of a Ca^{2+} wave (on the order of 100's of ms), a change of momentum can be on the order of 10^{-30} kg-m/s for a typical Ca^{2+} ion. A Ca^{2+} wave packet of 1000 ions with onset time of 1 ms, exerts a force on the order of 10^{-24} N (1 N $\equiv$ 1 Newton = 1 kg-m/s^2). A nano-robot would be attracted to this site, depositing chemicals/drugs that interact with the regenerative Ca^{2+}-wave process.

An area of the receptor of the nanosystem of 1 nm^2 would require pressure sensitivity of 10^{-6} Pa (1 Pa = 1 pascal = 1 N/m^2).

The nano-robot could be switched on/off at a regional/columnar level by sensitivity to local electric/magnetic fields. Highly synchronous firings during STM processes can be affected by these piezoelectric nanosystems which affect background/noise efficacies via control of Ca^{2+} waves. In turn, this would affect the influence of of Ca^{2+} waves via the vector potential $\mathbf{A}$, etc.

4.11 Free will

There is interest in researching possible quantum influences on highly synchronous neuronal firings relevant to STM to understand connections to consciousness and “Free Will” (FW) (Ingber, 2016a,b).

If experimental evidence is gained of quantum-level processes of tripartite synaptic interactions with large-scale synchronous neuronal firings, then FW may be established using the Conway-Kochen quantum no-clone “Free Will Theorem” (FWT) (Conway & Kochen, 2006, 2009).

The essence of FWT is that, since quantum states cannot be cloned, a Ca^{2+} quantum wave-packet may not generate a state proven to have previously existed. As explained by the authors (Conway & Kochen, 2006, 2009), experimenters have specific choices in selecting measurements, which are shared by (twinned) particles, including the choice of any random number generator that might be used to aid such choices. Those authors maintain that their proof and description of quantum measurements used is general enough to rule out classical randomness, and that classical determinism cannot be supported by such processes as exist in the quantum world.

4.12 Affective fits to EEG

The PI's current XSEDE.org grant is for “Affective Modulation of Information Processing During Attention Tasks”, basically using the same ASA and SMNI algorithms that were successful in modeling attention states, generalized to affective states.

5 Statistical Mechanics of Financial Markets (SMFM)

5.1 Trading in risk dimensions (TRD) & risk-management

Some of the author's previous work, mostly published, developed two-shell recursive trading systems. An inner-shell of trading indicators is adaptively fit to incoming market data. A parameterized trading-rule outer-shell uses the author's global optimization ASA code (Ingber, 1993a) to fit the trading system to historical data. A simple fitting algorithm, usually not requiring ASA, is used for the inner-shell fit.

Trading in Risk Dimensions (TRD) (Ingber, 2005, 2010a), adds an additional risk-management middle-shell to create a three-shell recursive optimization/sampling/fitting algorithm. Portfolio-level distributions of copula-transformed multivariate distributions (with constituent markets possessing different marginal distributions in returns space) are generated by Monte Carlo samplings. ASA is used to importance-sample weightings of these markets.

TRD processes Training and Testing trading systems on historical data, and consistently interacts with RealTime trading platforms – at all time resolutions, e.g., including high-frequency trading (HFT), minute, daily, monthly, etc. The code is written in vanilla C, and runs across platforms such as Windows/Cygwin, SPARC/Solaris, i386/FreeBSD, i386/NetBSD, etc. TRD can be run as an independent executable or called as a DLL.

TRD can robustly and flexibly interact with various trading platforms. The author has developed a working Windows interface with TradeStation and other Linux platforms.

The TRD code was used for HFT when the author was a Partner with PION Capital 2011-2013.

5.1.1 Copula transformation

Gaussian copulas are developed in TRD (Ingber, 2010a). Other copula distributions are possible, e.g., Student-t distributions (often touted as being more sensitive to fat-tailed distributions — here data is first adaptively fit to fat-tailed distributions prior to copula transformations). These alternative distributions can be quite slow because inverse transformations typically are not as quick as for the present distribution.

Copulas are cited as an important component of risk management not yet widely used by risk management practitioners (Blanco, 2005). Gaussian copulas are presently regarded as the Basel II standard for credit risk management (Horsewood, 2005). While real-time risk-management for intra-day trading is becoming more popular, most approaches still use simpler VaR measures (Dionne *et al.*, 2006). TRD permits fast as well as robust copula risk management in real time.

The copula approach can be extended to more general distributions than those considered here (Ibragimon, 2005). If there are not analytic or relatively standard math functions for the transformations (and/or inverse transformations described) here, then these transformations must be performed explicitly numerically in code such as TRD. Then, the ASA_PARALLEL OPTIONS already existing in ASA (developed as part of the 1994 National Science Foundation Parallelizing ASA and PATHINT Project (PAPP)) would be very useful to speed up real time calculations (Ingber, 1993a).

5.1.2 Transformation to Gaussian marginal distributions

A Normal Gaussian distribution has the form

$$p(dy) = \frac{1}{\sqrt{2\pi}} e^{-\frac{dy^2}{2}} \tag{55}$$

with a cumulative distribution

$$F(dy) = \frac{1}{2}\left[1 + \mathrm{erf}\left(\frac{dy}{\sqrt{2}}\right)\right] \tag{56}$$

where the erf() function is a tabulated function,

$$\mathrm{erf}(x) = \frac{2}{\sqrt{\pi}} \int_0^x dx' e^{-x'^2} \tag{57}$$

By setting the numerical values of the above two cumulative distributions, monotonic on interval [0,1], equal to each other, the transformation of the x marginal variables to the y marginal variables is effected,

$$\begin{aligned} dy &= \sqrt{2}\,\mathrm{erf}^{-1}\big(2\,F(dx) - 1\big) \\ &= \sqrt{2}\,\mathrm{sgn}(dx - m)\,\mathrm{erf}^{-1}\left(1 - e^{-\frac{|dx-m|}{\chi}}\right) \end{aligned} \tag{58}$$

The inverse mapping is used when applying this to the portfolio distribution. Note that

$$\begin{aligned} dy \geq 0 &\rightarrow dx - m \geq 0 \\ dy < 0 &\rightarrow dx - m < 0 \\ \mathrm{erf}([.]) &= -\mathrm{erf}(-[.]) \end{aligned} \tag{59}$$

yields

$$dx = m - \mathrm{sgn}(dy)\chi \ln\left[1 - \mathrm{erf}\left(\frac{|dy|}{\sqrt{2}}\right)\right] \tag{60}$$

5.1.3 Including correlations

To understand how correlations enter, look at the stochastic process defined by the dy^i marginal transformed variables:

$$dy^i = \hat{g}^i dw_i \tag{61}$$

where dw_i is the Wiener Gaussian noise contributing to dy^i of market i. The transformations are chosen such that $\hat{g}^i = 1$.

Now, a given market's noise, $(\hat{g}^i dw_i)$, has potential contributions from all N markets, which is modeled in terms of N independent Gaussian processes, dz_k,

$$\hat{g}^i dw_i = \sum_k \hat{g}^i_k dz_k \tag{62}$$

The covariance matrix $\left(g^{ij}\right)$ of these y variables is then given by

$$g^{ij} = \sum_k \hat{g}^i_k \hat{g}^j_k \tag{63}$$

with inverse matrix, the "metric," written as $\left(g_{ij}\right)$ and determinant of $\left(g^{ij}\right)$ written as g.

Since Gaussian variables are now being used, the covariance matrix is calculated directly from the transformed data using standard statistics, the point of this "copula" transformation (Malevergne & Sornette, 2002; Rosenberg & Schuermann, 2004).

Correlations ρ^{ij} are derived from bilinear combinations of market volatilities

$$\rho^{ij} = \frac{g^{ij}}{\sqrt{g^{ii} g^{jj}}} \tag{64}$$

Since the transformation to Gaussian space has defined $g^{ii} = 1$, here the covariance matrices theoretically are identical to the correlation matrices.

This transformation is rigorously enforced. I.e., a finite sample of Gaussian-transformed (pre-filtered) returns data will not yield a covariance matrix equal to its correlation matrix, so the covariance matrix is properly normalized (by dividing by the sqrt of the products of the diagonal elements). This step affords some statistical robustness of this procedure over moving windows of data.

This gives a multivariate correlated process P in the dy variables, in terms of Lagrangians L and Actions A,

$$P(dy) \equiv P(dy^1, ..., dy^N) = (2\pi dt)^{-\frac{N}{2}} g^{-\frac{1}{2}} e^{-Ldt} \tag{65}$$

where $dt = 1$ above. The Lagrangian L is given by

$$L = \frac{1}{2dt^2} \sum_{ij} dy^i g_{ij} dy^j \tag{66}$$

The effective action A_{eff}, presenting a "cost function" useful for sampling and optimization, is defined by

$$\begin{aligned} P(dy) &= e^{-A_{eff}} \\ A_{eff} &= Ldt + \frac{1}{2} \ln g + \frac{N}{2} \ln(2\pi dt) \end{aligned} \tag{67}$$

5.1.4 Stable covariance matrices

Covariance matrices, and their inverses (metric), are known to be quite noisy, so often they must be further developed/filtered for proper risk management. The root cause of this noise is recognized as "volatility of volatility" present in market dynamics, which essentially doubles the number of stochastic variables to consider (Ingber & Wilson, 1999). In addition to such problems, ill-conditioned matrices can arise from loss of precision for large variables sets, e.g., when calculating inverse matrices and determinants as required here. In general, the window size used for covariance calculations should exceed the number of market variables to help tame such problems.

A very good approach for avoiding ill-conditioning and lack of positive-definite matrices is to perform pre-averaging of input data using a window of three epochs (Litterman & Winkelmann, 1998). Other methods in the literature include subtracting eigenvalues of parameterized random matrices (Laloux *et al.*, 1999). Using Gaussian transformed data alleviates problems usually encountered with fat-tailed distributions. Selection of reasonable windows, coupled with pre-averaging, seems to robustly avoid ill-conditioning. This was tested in portfolios of 20-100 markets.

The covariance matrix of the historical [0, 1] Gaussian transformed exponentially distributed returns is to be used for forecasts of future returns. As mentioned in the previous section, after calculating the covariance matrix from an historical sample, it is renormalized to StdDevs of 1, i.e., defining the correlation matrix consistent with the theoretical transformation above.

The combination of moving-average windows, 3-epochs pre-averaging, and renormalization effectively gets rid of negative eigenvalues over all epochs of data.

5.1.5 Fitting data

Results must be tested with respect to WINDOW$_\chi$ sizes for updated covariance calculations, and with respect to using standard versus exponential moving averages. Tests should be performed regularly for ill-conditioned matrices.

5.1.6 Copula of multivariate correlated distribution

The multivariate distribution in x-space is specified, including correlations, using

$$P(dx) = P(dy) \left| \frac{\partial \, dy^i}{\partial \, dx^j} \right| \tag{68}$$

where $\left| \frac{\partial dy^i}{\partial dx^j} \right|$ is the Jacobian matrix specifying this transformation. This gives

$$P(dx) = g^{-\frac{1}{2}} e^{-\frac{1}{2} \sum_{ij} \left(dy^i_{dx}\right)^{\dagger} \left(g_{ij} - I_{ij}\right) \left(dy^j_{dx}\right)} \prod_i P_i(dx^i) \tag{69}$$

where $\left(dy_{dx}\right)$ is the column-vector of $\left(dy^1_{dx}, \ldots, dy^N_{dx}\right)$ expressed back in terms of their respective $\left(dx^1, ..., dx^N\right)$, $\left(dy_{dx}\right)^{\dagger}$ is the transpose row-vector, and $\left(I\right)$ is the identity matrix (all ones on the diagonal).

The Gaussian copula $C(dx)$ is defined from Eq. (0),

$$C(dx) = g^{-\frac{1}{2}} e^{-\frac{1}{2} \sum_{ij} \left(dy^i_{dx}\right)^{\dagger} \left(g_{ij} - I_{ij}\right) \left(dy^j_{dx}\right)} \tag{70}$$

5.2 PATHTREE, PATHINT & options

The author has developed a full suite of options codes, which may be integrated with TRD, or used independently.

In the early 1990's I developed PATHINT to evolve multivariate probability distributions, defined by general nonlinear Gaussian Markovian processes — multiplicative noise, and published applications in several disciplines. In 2000, I created a faster algorithm PATHTREE, a binomial tree to evolve such probability distributions. PATHTREE was thoroughly tested and finally published (Ingber *et al.*, 2001). Both PATHTREE and PATHINT have been applied to options codes, e.g., delivering full sets of Greeks based on such underlying probability distributions. Because of its speed of processing, PATHTREE has been used to fit the shape of distributions to strike data, i.e., a robust bottom-up approach to modeling dependence of strikes on volatilities. New codes, qPATHTREE and qPATHINT, have been developed for similar use in quantum complex-variable spaces under an XSEDE.org grant, "Quantum path-integral qPATHTREE and qPATHINT algorithm" (Ingber, 2016a, 2017a,b,c, 2018a,b,c). These codes have broad applications, e.g., ranging from computational neuroscience to computational physics to blockchains.

5.3 Financial options

The final product in each case, in addition to training use of calculated indicators, would be a full set of options Greeks. There are necessary indicators for the use of options. For a portfolio Π containing an option and its underlying S with volatility σ, the algebra of "Greeks" is summarized as (Ingber, 2002)

$$\begin{aligned} d\Pi = {} & \frac{\partial \Pi}{\partial S} dS + \frac{1}{2} \frac{\partial^2 \Pi}{\partial dS^2} dS^2 + \frac{\partial \Pi}{\partial \sigma} d\sigma + \frac{\partial \Pi}{\partial t} dt \\ & + \frac{\partial^2 \Pi}{\partial S \, \partial \sigma} dS \, d\sigma + \frac{1}{2} \frac{\partial^2 \Pi}{\partial \sigma^2} d\sigma^2 + \frac{1}{6} \frac{\partial^3 \Pi}{\partial S^2 \, \partial \sigma} dS^2 \, d\sigma + \ldots \end{aligned} \tag{71}$$

translating to

$$
\begin{aligned}
d\Pi = \Delta\, dS + \frac{1}{2}\Gamma\, dS^2 + K\, d\sigma + \Theta\, dt \\
+ \Delta'\, dS\, d\sigma + \frac{1}{2}K'\, d\sigma^2 + \frac{1}{6}\Gamma'\, dS^2\, d\sigma + \dots
\end{aligned}
\tag{72}
$$

Note that since probability distributions are an integral component of options calculations, for some projects this may require interviews of experts to gather data.

5.4 Other portfolios

5.4.1 Portfolio of physiological indicators (PPI)

Quite general portfolios of specialized constituents also can be addressed. For example, multiple synchronous imaging data, processed with the TRD copula risk analysis, and using SMNI models (Ingber, 1982, 1983, 2008a). leads to a portfolio of physiological indicators (PPI) to enhance resolution of neocortical processing information (Ingber, 2006a).

5.4.2 Ideas by statistical mechanics (ISM)

"Ideas by Statistical Mechanics (ISM)", integrates previous projects to model evolution and propagation of ideas/patterns throughout populations subjected to endogenous and exogenous interactions (Ingber, 2006b, 2007a, 2008b). This product can be used for decision support for projects ranging from diplomatic, information, military, and economic (DIME) factors of propagation/evolution of ideas, to commercial sales, trading indicators across sectors of financial markets, advertising and political campaigns, etc.

5.4.3 Real options for project schedules (ROPS)

Similar tools can be applied to price complex projects as financial options with alternative schedules and strategies. PATHTREE processes real-world options, including nonlinear distributions and time-dependent starting and stopping of sub-projects, with parameters of shapes of distributions fit using ASA to optimize cost and duration of sub-projects (Ingber, 2007b, 2010b).

5.5 Developing bid-ask probabilities for high-frequency trading

Although high-frequency trading (HFT) is a relatively new development in financial markets, it has become a primary force in market pricing. A large scientific literature has developed to understand the nature of these forces (Ait-Sahalia & Saglam, 2017; Avellaneda & Stoikov, 2008; Baradely *et al.*, 2018; Cartea *et al.*, 2014; Cont, 2011; Cont *et al.*, 2009; Fodra & Labadie, 2012; Gueant, 2017; Huang *et al.*, 2014).

Since HFT by definition implies fast trading, this has generally prevented complex sophisticated algorithms from being applied to trading in real time. This discussion shows how complex algorithms can be developed, with parameters optimized by the use of simulated annealing, to produce code that can be used in real time (Ingber, 2020a).

In this context, this description applies a previously developed statistical mechanics of financial markets (SMFM) (Ingber, 1984b, 1990, 1996a,b, 2000, 2010a, 2017b; Ingber *et al.*, 2001; Ingber & Mondescu, 2001, 2003; Ingber *et al.*, 1991b; Ingber & Wilson, 1999, 2000), here applied to developing joint bid-ask probabilities to high-frequency data, using two methods of fitting price data or returns data to (a) the distribution and (b) fitting the returns. The returns are also developed into closed-form algebra using the path-integral formalism.

The algebraic and numerical algorithms used here also have been applied to systems in other disciplines, e.g., neuroscience (Ingber, 1991, 1992, 1996c, 1997a, 1998a, 2006a, 2009a,b, 2012b,c, 2015a, 2018a,b,c; Ingber & Nunez, 1995, 2010; Ingber *et al.*, 2014, 1996; Nunez *et al.*, 2013) and combat simulations (Ingber, 1993b, 1998b). utilizing the ASA C-code (Ingber, 1993a, 1996d, 2012a).

As was true for these other disciplines, here too the path-integral methodology is used to develop canonical momenta indicators (CMI), useful to forecast direction and strengths of these variables.

5.5.1 Forecast code

Tick data was cleaned on-the-fly in C code, since this is a practical real-time consideration. The data was volume-weighted, and level-weighted by 0.9, using 20 levels each of bid and ask; the last level was weighted by $0.9^{20} = 0.122$.

It is clear that in many HFT markets such as the one used for this study, competitive traders' tactics, that "game" the book of bids and asks, cause the volume at different levels to be much more volatile than the prices

At first, both prices S and returns R of bids and asks were fit. The returns are simply

$$R(t) = S(t)/S(t-1) \tag{73}$$

Since the trends are the first entities to be swallowed by such markets, making them useless for trading, the ASA fits had to work longer for fits with prices than with returns, so returns were used for most of the runs.

5.5.2 Analytic returns

The path integral formalism permits an analytic calculation of the most probable state (Dekker, 1980),

$$dM^G/dt = g^G - g^{1/2}(g^{-1/2}g^{GG'})_{,G'} \tag{74}$$

5.5.3 MAXIMA to C code

The 2-factor functional forms used, with ask as x^1 and bid as x^2, are indexed here by j, without the Einstein convention,

$$\begin{aligned} g^j &= A_j + B_j\, x^j \\ \hat{g}^j_j &= C_j + D_j\, x^j \\ \hat{g}^1_2 &= E_1, \hat{g}^2_1 = E_2 \end{aligned} \tag{75}$$

where the parameters $\{A_i, B_i, C_i, D_i, E_i\}$ are fit to the data. Note that these simple functional forms, especially after inverses of the covariance matrix are taken, form Pade approximates, ratios of polynomials, known to be quite robust functional forms to fit data.

The cost function used is the effective Action, including the normalization,

$$A_{eff} = Ldt + N\log(2\pi dt)/2 + \log(g)/2 \tag{76}$$

A_{eff} the analytic expression above for returns can be calculated using the algebraic language Maxima. Since such expressions can be about 1000 characters (without spaces), this is advisable.

It is straightforward to convert Maxima output to Fortran code, but not so easy to covert to C. Previous projects have used f2c from netlib.org to compile mixed C and Fortran code, but here the main issue is that C requires powers to use the prefix operator-function pow(), whereas Maxima uses postfix operators. This was circumvented simply by writing all powers as multiple factors with different names, converting to Fortran, then renaming these the same after the calculations.

5.5.4 Dynamic memory

Arrays for books of data over a day or more require 10's of megabytes of memory. Static arrays that size crashes C code, so dynamic memory using calloc() was used.

5.5.5 Sampling code

It is not necessary to use all tick data to get very good fits. Instead, a modification of ASA subroutines that calculate random states was used to randomly sample the data that is already volume-weighted and level-weighted. It was found that a sample size of 100K gave as good results as a sample size of several million for a day of BitMEX data. This random sample then was used for the ASA cost function calculations that ran over the sample for each generated state.

5.5.6 Windows of data

The calculated distribution at any point is dependent on at least 2 points of weighted bid-ask data, and the calculation takes into account correlations and dynamics inherent in the functional form of the drifts and diffusions.

Therefore, the best use of this approach is to use narrow and wide windows for forecasting (Ingber & Mondescu, 2001). Although similar to a standard practice of using windows of raw data, the result is a different than would be calculated just using of raw incoming data (also volume-weighted and level-weighted), since results include most probable correlated future behavior of the market.

If A_{eff} is fit directly, then the derived return equations were only accurate to a give dt, e.g., about 0.1 sec,, in agreement with the expected mesh used in PATHINT as described above, so instead returns were directly fit to future return data, typically requiring a few million ASA generated states, by “looking ahead” to the next dt point, Of course, PATHINT could be used to fold over the short-time distribution for many secs (as has been done in other systems), but most likely this would too slow in the context of HFT.

If the returns are fit directly to the data, then just about any dt, ranging from 0.1 sec to 5 sec give the same forecast value for given current data (returns are transformed back into prices — 6 significant figures), since a realistic set of fitted drifts and diffusion matrices can have parameters slip some from their ideal-dt range to still get good fits at another dt, and then the probability calculation at any given point just reflects essentially the same distribution.

5.5.7 *dt* library

A dt library is easily created, within a desired range of dt's that are “reasonably” close to the ideal-dt, by doing multiple ASA fits to return data. This defines a library of probabilities that can be used as described here, yielding a range of choices to be made during HFT, e.g., as required to take into account latencies of trades actually being posted.

5.5.8 Updating parameters

Fitted parameters can be updated overnight with new ASA runs. Alternatively, e.g., if there is a sudden change in context of the market and if sufficient recent data of the new context is available, the fast modified Nelder-Mead simplex code that comes with the ASA code typically used to efficiently gain some precision in fits, can be used to quickly update the parameters.

5.5.9 CMI

The forecast also includes the CMI. However, similar to limitations in fitting A_{eff}, which cannot be fit directly to the returns data for any dt, here too the forecast CMI at a different dt than ideal-dt need to have more ASA generated states for additional precision to get stable CMI (which often are useful guides on upcoming directions and strengths of bids, ask, midprices, etc.).

5.5.10 Volatility risk

The risk associated with the probability distributions were straightforwardly calculated from the covariance matrix $g^{GG'}$. A quick measure is its determinant g.

5.5.11 Discussion

A 2-factor probability distribution of bid-ask tick data was developed using Maxima to further develop C code. After parameters of the 2-factor drifts and diffusion matrix were fit, very fast calculations of narrow and wide windows of data are processed that are useful for high-frequency trading.

This thereby shows how complex algorithms may be used in HFT, using open-source tools like Maxima and ASA.

6 Statistical Mechanics of Combat (SMC)

A paper discusses SMC in more detail (Ingber, 1993b).

Preprints (www.preprints.org) | NOT PEER-REVIEWED | Posted: 8 October 2020 doi:10.20944/preprints202009.0385.v2

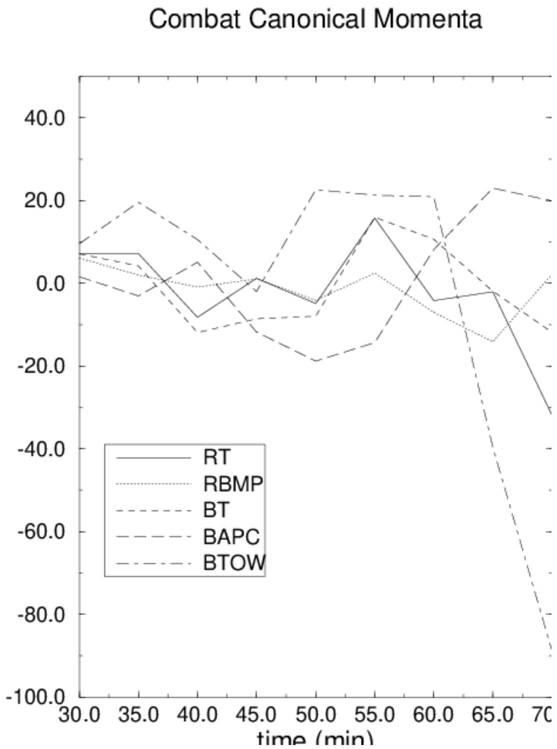

Fig. 6. The results of Janus(t) attrition of Red and Blue units are given in the upper figure. The canonical momenta indicators (CMI) for each system are given in the lower figure.

6.1 Necessity of comparing computer models to exercise data

This project addresses the utility of establishing a mathematical approach to compare exercise data to large scale computer models whose underlying microscopic interactions among men and machines are driven by the natural laws of physics. In this study, the focus is to compare the Janus(t) wargame to National Training Center (NTC) data, since both systems then take into account human interactions.

It also should be noted that "large scale" here refers to battalion level. (Army systems scale by factors of 3-5, from company to battalion to brigade to division to corps to army.) If these battalion level computer models can be favorably compared, and if consistency can be achieved between the hierarchy of large scale battalion level, larger scale corps level, and largest scale theater level computer models, then these higher echelon computer models also can be favorably compared. This could only enhance the value of training on these higher echelon computer models (Bartlett, 1988).

The requirement of depending more and more on combat computer models (including simulations and wargames) has been brought into sharper focus because of many circumstances, e.g.: (1) the nonexistence of ample data from previous wars and training operations, (2) the rapidly shortening time scale on which tactical decisions must be made, (3) the rapidly increasing scale at which men and machines are to be deployed, (4) the increasing awareness of new scenarios that are fundamentally different from historical experiences, (5) and the rapidly increasing expense of conducting training exercises.

Furthermore, such computer models could be used to augment training. We now spend several million dollars to cycle each battalion through NTC. The training of these commanders could be greatly enhanced if inexpensive pre and post training wargames were provided that statistically replicate their training missions. Even, or rather especially, for the development of such training aids, proper analysis and modeling is required to quantitatively demonstrate that the computer models are good statistical representations of the training mission.

6.2 Need for data

With the present development of high quality simulators (essentially computer simulations coupled with hardware to simulate close to actual machinery and communication) to augment training in the field, e.g., SIMNET, it should become increasingly important to "validate" the simulator system to some reality, even if only exercise reality. For example, several hundred simulators are likely to be driven in the context of tens of thousands of units being simulated by software similar to present-day computer simulations. In fact, many people see the necessity of integrating simulations and simulators to properly augment training. Thus, the semi-automated forces (SAF) driving the simulators must be validated.

6.3 Janus computer simulation of National Training Center

6.4 Description of National Training Center

The U.S. Army National Training Center (NTC) is located at Fort Irwin, just outside Barstow, California. As of 1989, there have been about 1/4 million soldiers in 80 brigade rotations at NTC, at the level of two battalion task forces (typically about 3500 soldiers and a battalion of 15 attack helicopters), which train against two opposing force (OPFOR) battalions resident at NTC. NTC comprises about 2500 km^2, but the current battlefield scenarios range over about 5 km linear spread, with a maximum lethality range of about 3 km. NTC is gearing up for full brigade level exercises.

Observer-controllers (OC) are present at various levels of command down to about platoon level. A rotation can have three force-on-force missions and one live-fire mission. OPFOR platoon and company level personnel are trained as US Army soldiers; higher commanders practice Soviet doctrine and tactics. An OPFOR force typically has carriers (BMPs) and

The primary purpose of data collection during an NTC mission is to patch together an after action review (AAR) within a few hours after completion of a mission, giving feedback to a commander who typically must lead another mission soon afterward. Data from the field, i.e., multiple integrated laser engagement system (MILES) devices, audio communications, OCs, and stationary and mobile video cameras, is sent via relay stations back to a central command center where this all can be recorded, correlated and abstracted for the AAR. Within a couple of weeks afterwards, a written review is sent to commanders, as part of their NTC take home package. It now costs about 4×10^6 dollars per NTC rotation, 1 million of which goes for this computer support.

There are 460 MILES transponders available for tanks for each battle. The B units have transponders, but most do not have transmitters to enable complete pairings of kills targets to be made. (New MILES devices being implemented have transmitters which code their system identification, thereby greatly increasing the number or recordings of pairings.) Thus, MILESs without transmitters cannot be tracked. Man packs with B units enable these men to be tracked, but one man pack can represent an aggregate of as many as five people.

B units send data to A stations (was 48, though 68 can be accommodated), then collected by two C stations atop mountains, and sent through cables to central VAXs forming a core instrumentation system (CIS). There is a present limitation of 400 nodes in computer history for video tracking (but 500 nodes can be kept on tape). Therefore, about 200 blue and 200 OPFOR units are tracked.

By varying the laser intensity and focusing parameters, a maximum laser-beam spread is achieved at the nominal range specified by the Army. A much narrower beam can reach as far as the maximum range. Focusing and attenuation properties of the laser beam makes these nominal and maximum ranges quite sharp, with resolution supposedly considerably less than several hundred meters under ideal environmental conditions.

With increasing demands to make training more realistic, the MILES devices need to be upgraded. For example, degradation of the laser beam under conditions of moderate to heavy smoke and dust might be at least partially offset by sending fewer words per message. New sensor abilities to encode specific shooters can also greatly aid data collection.

It should be understood that present training problems at NTC, e.g., training commanders — especially at Company level — to handle synchronization of more than three tasks, misuse of weapons systems, etc., overshadow any problems inherent in the MILES systems. We repeatedly have expressed this view for well over a year, after going to NTC several times; but only at a meeting at Carlisle Barracks, PA, on May 17, 1989, when various school commanders briefed Gen. Maxwell Thurman, TRADOC Commander, was this view broadly accepted.

6.5 Description of Janus(t)

Janus(t) is an interactive, two-sided, closed, stochastic, ground combat computer simulation. As discussed below, Janus(t) has been expanded to include air and naval combat, in several projects with the author's previous thesis students at the Naval Postgraduate School (NPS).

Interactive refers to the the fact that military analysts (players and controllers) make key complex decisions during the simulation, and directly react to key actions of the simulated combat forces. Two-sided (hence the name Janus of the Greek two-headed god) means that there are two opposing forces simultaneously being directed by two set of players. Closed means that the disposition of the enemy force is not completely known to the friendly forces. Stochastic means that certain events, e.g., the result of a weapon being fired or the impact of an artillery volley, occur according to laws of chance [random number generators and tables of probabilities of detection (PD), acquisition (PA), hit (PH), kill (PK), etc.]. The principle modeling focus is on those military systems that participate in maneuver and artillery operations. In addition to conventional direct fire and artillery operations, Janus(t) models precision guided munitions, minefield employment and breaching, heat stress casualties, suppression, etc.

6.6 Mathematical formalism

Consider a scenario taken from this NTC study: two red systems, red T-72 tanks (RT) and red armored personnel carriers ($RBMP$), and three blue systems, blue M1A1 and M60 tanks (BT), blue armored personnel carriers ($BAPC$), and blue tube-launched optically-tracked wire-guided missiles ($BTOW$), where RT specifies the number of red tanks at a given time t, etc. Consider the kills suffered by BT, ΔBT, e.g., within a time epoch $\Delta t \approx 5$ min.

$$\begin{aligned} \frac{\Delta BT}{\Delta t} &\equiv \dot{BT} \\ &= x^{BT}_{RT} RT + y^{BT}_{RT} RT\, BT + x^{BT}_{RBMP} RBMP + y^{BT}_{RBMP} RBMP\, BT \\ &\quad + z^{BT}_{BT} BT \eta^{BT}_{BT} + z^{BT}_{RT} \eta^{BT}_{RT} + z^{BT}_{RBMP} \eta^{BT}_{RBMP} \end{aligned} \tag{77}$$

Here, the x terms represent attrition owing to point fire; the y terms represent attrition owing to area fire. Note that the algebraic forms chosen are consistent with current perceptions of aggregated large scale combat. Sources of noise, e.g., arise from PD, PA, PH, PK, etc. Furthermore, such noise likely has its own functional dependencies, e.g., possibly being proportional to the numbers of units involved in the combat. The η represent sources of (white) noise (in the ItThe noise terms are taken to be log normal (multiplicative) noise for the diagonal terms and additive noise for the off-diagonal terms. The diagonal z term (z^{BT}_{BT}) represents uncertainty associated with the z terms represent uncertainty associated with the RT and $RBMP$. The x and y are constrained such that each term is bounded by the mean of the KVS, averaged over all time and trajectories of similar scenarios; similarly, each z term is constrained to be bounded by the variance of the KVS. The methodology presented here can accommodate any other nonlinear functional forms, and any other variables that can be reasonably represented by such rate equations, e.g., expenditures of ammunition or bytes of communication (Ingber, 1989b). Variables that cannot be so represented, e.g., terrain, C3, weather, etc., must be considered as "super-variables" that specify the overall context for the above set of rate equations.

Equations similar to the $\dot{BT}$ equation are also written for $\dot{RT}$, $\dot{RBMP}$, $\dot{BAPC}$, and $\dot{BTOW}$. Only x and y that reflect possible nonzero entries in the KVS are free to be used for the fitting procedure. For example, since Janus(t) does not permit direct-fire fratricide, such terms are set to zero. In most NTC scenarios, fratricide typically is a very small effect. Nondiagonal noise terms give rise to correlations in the covariance matrix. Thus,

$$\begin{aligned} M^G &= \{RT, RBMP, BT, BAPC, BTOW\} \\ \dot{M}^G &= g^G + \sum_i \hat{g}^G_i \eta^i \\ \hat{g}_i &= z^G_i M^G, , i = G \\ \hat{g}_i &= z^G_i, , i \neq G \end{aligned} \tag{78}$$

6.7 Problems in Lanchester theory

Quasilinear deterministic mathematical modeling is not only a popular theoretical occupation, but many wargames, e.g., joint Theater Level Simulation (JTLS), use such equations as the primary algorithm to drive the interactions between opposing forces.

In its simplest form, this kind of mathematical modeling is known as Lanchester theory:

$$\begin{aligned} \dot{r} &= \mathrm{d}r/\mathrm{d}t = x_r b + y_r r b \\ \dot{b} &= \mathrm{d}b/\mathrm{d}t = x_b r + y_b b r \end{aligned} \tag{79}$$

where r and b represent red and blue variables, and the x and y are parameters that somehow should be fit to actual data.

It is well known, or should be well known, that it is notoriously difficult, if not impossible, to use the simple Lanchester equations to mathematically model any real data with any reasonable degree of precision. These equations perhaps are useful to discuss some gross systematics, but it is discouraging to accept that, for example, a procurement decision involving billions of dollars of national resources could hinge on mathematical models dependent on Lanchester theory.

Some investigators have gone further, and amassed historical data to claim that there is absolutely no foundation for believing that Lanchester theory has anything to do with reality (Dupuy, 1987). However, although there is some truth to the above criticisms, the above conclusions do not sit comfortably with other vast stores of human experience. Indeed, this controversy is just one example that supports the necessity of having human intervention in the best of plans, no matter how (seemingly) sophisticated analysis supports conclusions contrary to human judgment (vanCreveld, 1985).

6.8 Numerical implementation

6.8.1 Fitting parameters

The five coupled stochastic differential equations, for variables $M^G = \{RT, RBMP, BT, BAPC, BTOW\}$, can be represented equivalently by a short-time conditional probability distribution P in terms of a Lagrangian L:

$$P(R\cdot, B\cdot; t + \Delta t | R\cdot, B\cdot; t) = \frac{1}{(2\pi\Delta t)^{5/2}\sigma^{1/2}} \exp(-L\Delta t) \tag{80}$$

where σ is the determinant of the inverse of the covariance matrix, the metric matrix of this space, "$R\cdot$" represents $\{RT, RBMP\}$, and "$B\cdot$" represents $\{BT, BAPC, BTOW\}$. (Here, the prepoint discretization is used, which hides the Riemannian corrections explicit in the midpoint discretized Feynman Lagrangian; only the latter representation possesses a variational principle useful for arbitrary noise.)

This defines a scalar "dynamic cost function," $C(x, y, z)$,

$$C(x, y, z) = L\Delta t + \frac{5}{2}\ln(2\pi\Delta t) + \frac{1}{2}\ln\sigma \tag{81}$$

which can be used with the very fast simulated reannealing (VFSR) algorithm (Ingber, 1989a) further discussed below, to find the (statistically) best fit of $\{x, y, z\}$ to the data.

The form for the Lagrangian L and the determinant of the metric σ to be used for the cost function C is

$$\begin{aligned} L &= \sum_G \sum_{G'} \frac{(\dot{M}^G - g^G)(\dot{M}^{G'} - g^{G'})}{2g^{GG'}} \\ \sigma &= \det(g_{GG'}) \\ (g_{GG'}) &= (g^{GG'})^{-1} \\ g^{GG'} &= \sum_i \hat{g}_i^G \hat{g}_i^{G'} \end{aligned} \tag{82}$$

Generated choices for $\{x, y, z\}$ are constrained by empirical KVSs (taken from exercises or from computer simulations of these exercises)

$$\begin{aligned} g^G(t) &\le n^G < \Delta M^G(t) > \\ \hat{g}_i^G(t) &\le n_i^G \left[< \left(\Delta M^G(t)\right)^2 > \right]^{1/2} \end{aligned} \tag{83}$$

where n^G and n_i^G are the number of terms in g^G and $\hat{g}_i^G$, respectively, and averages $< \cdot >$ are taken over all time epochs and trajectories of similar scenarios.

If there are competing mathematical forms, then it is advantageous to use the path integral to calculate the long-time evolution of P (Ingber, 1989b). Experience has demonstrated that, since P is exponentially sensitive to changes in L, the long-time correlations derived from theory, measured against the empirical data, is a viable and expedient way of rejecting models not in accord with empirical evidence.

Note that the use of the path integral is a posteriori to the short-time fitting process, and is a subsidiary physical constraint on the mathematical models to judge their internal soundness and suitability for attempts to extrapolate to other scenarios.

6.8.2 Combat power scores

After the $\{x, y, z, \}$ are fit to the data and a mathematical model is selected, another fit can be superimposed to find the effective "combat scores," defined here as the relative contribution of each system to the specific class of scenarios in question. Using a fundamental property of probability distributions, a probability distribution $P_A(q)$ of aggregated variables $q_1 + q_2$ can be obtained from the probability distribution for $P(q_1, q_2)$

$$P_A(q = q_1 + q_2) = \int \mathrm{d}q_1 \, \mathrm{d}q_2 \, P(q_1, q_2) \delta(q - q_1 - q_2) \tag{84}$$

where $\delta(\cdot)$ is the Dirac delta function.

Thus, the aggregated conditional probability is calculated

$$\begin{aligned} & P_A(r, b; t + \Delta t | R\cdot, B\cdot; t) \\ &= \int \mathrm{d}RT \, \mathrm{d}RBMP \, \mathrm{d}BT \, \mathrm{d}BAPC \, \mathrm{d}BTOW \, P(R\cdot, B\cdot; t + \Delta t | R\cdot, B\cdot; t) \\ & \times \delta(r - w^r_{RT} RT - w^r_{RBMP} RBMP) \\ & \times \delta(b - w^b_{RT} BT - w^b_{BAPC} BAPC - w^b_{BTOW} BTOW) \end{aligned} \tag{85}$$

where the w represent the desired combat scores. After the $\{x, y, z\}$ have been fitted, the new parameters $\{w\}$ can be fit to the data by maximizing the cost function $C'(w)$ using VFSR,

$$C'(w) = -\ln P_A \tag{86}$$

Note that the simple linear aggregation by systems above can be generalized to nonlinear functions, thereby taking into account synergistic interactions among systems that contribute to overall combat effectiveness.

It is possible to include human factors in combat power scores, by including human-factors variables in such equations (Ingber & Sworder, 1991).

6.8.3 Modeling of National Training Center

The "kills" attrition data from NTC and the Janus(t)/NTC simulation at once looks strikingly similar during the force-on-force part of the combat.

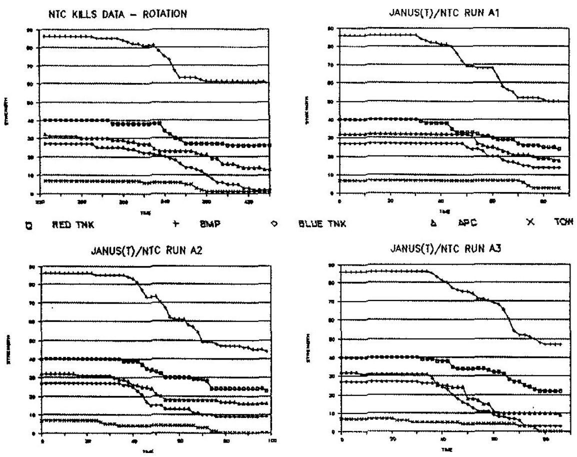

Fig. 7. NTC vs Janus(t), attrition ("kills") data for an NTC mission (upper left box) and for three Janus(t) runs using the NTC qualified database.

Note that this fits only half the middle part of the engagement, where the slope of attrition is very steep (and almost linear on the given scale), i.e., the "force on force" part of the engagement. The second half of the data must be predicted by the models.

From the single NTC trajectory qualified to date, seven 5-min intervals in the middle of the battle were selected. From six Janus(t) runs, similar force-on-force time epochs were identified, for a total of 42 data points. In the following fits, r represents red tanks, and b represents blue tanks.

Fitting NTC data to an additive noise model, a cost function of 2.08 gave

$$\begin{aligned}\dot{r} &= -2.49 \times 10^{-5} b - 4.97 \times 10^{-4} br + 0.320 \eta_r \\ \dot{b} &= -2.28 \times 10^{-3} r - 3.23 \times 10^{-4} rb + 0.303 \eta_b \end{aligned} \tag{87}$$

Fitting NTC data to a multiplicative noise model, a cost function of 2.16 gave

$$\begin{aligned}\dot{r} &= -5.69 \times 10^{-5} b - 4.70 \times 10^{-4} br + 1.06 \times 10^{-2} (1 + r) \eta_r \\ \dot{b} &= -5.70 \times 10^{-4} r - 4.17 \times 10^{-4} rb + 1.73 \times 10^{-2} (1 + b) \eta_b \end{aligned} \tag{88}$$

Fitting Janus(t) data to an additive noise model, a cost function of 3.53 gave

$$\begin{aligned}\dot{r} &= -2.15 \times 10^{-5} b - 5.13 \times 10^{-4} br + 0.530 \eta_r \\ \dot{b} &= -5.65 \times 10^{-3} r - 3.98 \times 10^{-4} rb + 0.784 \eta_b \end{aligned} \tag{89}$$

Fitting Janus(t) data to a multiplicative noise model, a cost function of 3.42 gave

$$\begin{aligned}\dot{r} &= -2.81 \times 10^{-4} b - 5.04 \times 10^{-4} br + 1.58 \times 10^{-2} (1 + r) \eta_r \\ \dot{b} &= -3.90 \times 10^{-3} r - 5.04 \times 10^{-4} rb + 3.58 \times 10^{-2} (1 + b) \eta_b \end{aligned} \tag{90}$$

This comparison illustrates that two different models about equally fit the short-time distribution. The multiplicative noise model shows that approximately a factor of 100 of the noise might be "divided out," or understood in terms of the physical log normal mechanism.

To discern which model best fits the data, the path integral calculation of the long-time distribution is used to see which model best follows the actual data.

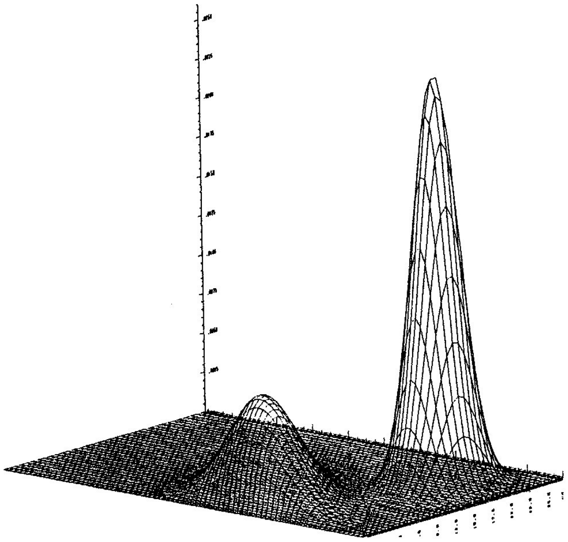

Fig. 8. Path integral calculation of long-time distribution: The horizontal axes represent red and blue forces. For this Janus(t) additive noise case, two time slices are superimposed. Taking the initial onset of the engagement as 35 minutes, these peaks represent 50 and 100 minutes.

In general, the probability can be a highly nonlinear algebraic function, and there will be multiple peaks and valleys.

Since only one NTC mission was qualified, the variance of deviation from the mean is not really significant; it is given only to illustrate the author's approach that can be applied to more NTC missions as they are qualified and aggregated. Note that only the blue Janus(t) variances of the additive noise model are consistent with the NTC data.

6.9 Discussion

Data from 35 to 70 minutes was used for the short-time fit. The path integral code was used to calculate the long-time evolution of this fitted short-time (5-min) distribution from 35 to beyond 70 min. This serves to compare long-time correlations in the mathematical model vs the data, and to help judge extrapolation past the data used for the short-time fits. More data and work are required to find a better (or best?) algebraic form. The resulting form is required for input into higher echelon models. As more NTC data becomes available (other NTC missions are in the process of being qualified, wargamed, and analyzed), it can be possible to judge the best models with respect to how well they extrapolate across slightly different combat missions.

7 Applications to COVID-19

It is generally recognized that the spread of COVID-19 is affected by multiple variables, e.g., potentially including ethnicity, population density, obesity, deprivation, pollution, race, environmental temperature (Anastassopoulou *et al.*, 2020; Bray *et al.*, 2020; Li *et al.*, 2020). Also, the Centre for Evidence-Based Medicine (CEBM) regularly cites papers on the dynamics of COVID-19 at https://www.cebm.net/evidence-synthesis/transmission-dynamics-of-covid-19/ .

This work offers the application of two basic multivariate algorithms to fairly generic issues in forecasting. As such, they may be useful to fit COVID-19 data and to help predict upcoming spread and control of this pandemic.

> (a) Adaptive Simulated Annealing (ASA) is an importance-sampling optimization code usually used for nonlinear, nonequilibrium, non-stationary, multivariate systems.
>
> (b) PATHINT is a numerical path-integral PATHINT code used for propagation of nonlinear probability distributions, including discontinuities.

These codes were developed by the author and applied across multiple disciplines.

There is not "one size fits all" in forecasting different systems. This was demonstrated for three systems (Ingber, 2020b), where the author has addressed multiple projects across multiple disciplines using these tools: 72 papers/reports/lectures in neuroscience, e.g. (Ingber, 2018a, 2020c), 31 papers/reports/lectures in finance, e.g. (Ingber, 2020a; Ingber & Mondescu, 2003), 24 papers/reports/lectures in combat analyses, e.g. (Ingber, 1993b, 2015b), and 11 papers/reports/lectures in optimization, e.g. (Atiya *et al.*, 2003; Ingber, 2012a), . It is reasonable to expect that this approach can be applied to many other projects.

For example, the path-integral representation of multivariate nonlinear stochastic differential equations permits derivation of canonical momenta indicators (CMI) which are faithful to intuitive concepts like Force, Momenta, Mass, etc (Ingber, 1996a, 2015b; Ingber & Mondescu, 2001). Correlations among variables are explicitly included in the CMI.

7.1 Data

A large and updated database for COVID-19 is maintained by the Centers for Disease Control and Prevention (CDC) at https://www.cdc.gov/library/researchguides/2019novelcoronavirus/researcharticles.html and at https://www.cdc.gov/library/researchguides/2019novelcoronavirus/datastatistics.html .

It is noted that EEG changes are observed by COVID-19 patients (Pasini *et al.*, 2020). EEG may provide a reasonable diagnostic tool.

7.2 Technical considerations

If there is not time to process large data sets, then the data can be randomly sampled, e.g., as described in another paper, "Developing bid-ask probabilities for high-frequency trading" (Ingber, 2020a).

If the required forecast is longer than the conditional distribution can sustain, PATHINT/PATHTREE can be used to propagate the distribution.

The dataset should be broken into independent Training and Testing subsets, to test the trained distribution. If this is not possible, e.g., because of data or time limitations, at the least experts can be used to judge if the model is ready for real-time applications, e.g., the Delphi method (Okoli & Pawlowski, 2004).

If an algorithm like ASA is to be used across a large class of problems, then it must be tunable to different classes. Over the 30+ years of ASA development, the author has worked with many volunteers who have contributed valuable ideas, modifications and corrections to this code. This has resulted in over 150 ASA options that can be used for additional timing additional tuning making it useful across many classes of problems.

The path integral algorithm includes its mathematical equivalents, a large class of stochastic differential equations and a large class of partial differential equations. The advantages of the path integral algorithm are:

> (a) intuitive description in terms of classical forces, inertia, momentum, etc., leading to new indicators.
>
> (b) delivering a cost function derived from a Lagrangian, or its Action (Lagrangian x dt). Sometimes constraints need to be added as Lagrange multipliers, as was required for normalization requirements in financial risk projects (Ingber, 2010a).

7.3 Summary

Two algorithms are suggested for fitting data and forecasting COVID-19, ASA for importance-sampling and fitting parameters to models, and PATHINT/PATHTREE. These algorithms have been applied to several disciplines — neuroscience, financial markets, combat analysis. While optimization and path-integral algorithms are now quite well-known (at least to many scientists), these previous applications give strong support to application of these tools to COVID-19 data.

8 Conclusion

A basic description of two algorithms is given, ASA for importance-sampling and fitting parameters to models, and PATHINT/PATHTREE (and their quantum analogs qPATHINT/qPATHTREE). Following are three main sections describing forecasting in three quite disparate disciplines — neuroscience, financial markets, combat analysis — using these basic algorithms. While optimization and path-integral algorithms are now quite well-known (at least to many scientists), these applications give strong support to a quite generic application of these tools to stochastic nonlinear systems.

Applications have been described to use these algorithms for forecasting the spread of COVID-19, and EEG may provide a reasonable diagnostic tool.

Acknowledgment

The author thanks the Extreme Science and Engineering Discovery Environment (XSEDE.org), for supercomputer grants since February 2013. The PI has held yearly grants for supercomputer resources from XSEDE, mostly for work on SMNI but for a couple years also to develop qPATHINT and qPATHTREE codes for propagation of quantum wave functions in the presence of random shocks.

References

Agulhon, C., Petravicz, J., McMullen, A., Sweger, E., Minton, S., Taves, S., Casper, K., Fiacco, T., McCarthy, K. (2008). What is the role of astrocyte calcium in neurophysiology? *Neuron* 59, 932–946.

Ait-Sahalia, Y., Saglam, M. (2017). High frequency market making: Optimal quoting. Technical Report SSRN_ID2986523_code758570, Princeton U., Princeton, NJ. `http://dx.doi.org/10.2139/ssrn.2331613`.

Anastassopoulou, C., Russo, L., Tsakris, A., Siettos, C. (2020). Data-based analysis, modelling and forecasting of the COVID-19 outbreak. *Public Library of Science One* 15(3). `https://doi.org/10.1371/journal.pone.0230405`.

Araque, A., Navarrete, M. (2010). Glial cells in neuronal network function. *Philosophical Transactions of The Royal Society B* , 2375–2381.

Asher, J. (2012). Brain's code for visual working memory deciphered in monkeys NIH-funded study. Technical Report NIH Press Release, NIH, Bethesda, MD. `http://www.nimh.nih.gov/news/science-news/2012/in-sync-brain-waves-hold-memory-of-objects-just-seen.shtml`.

Atiya, A., Parlos, A., Ingber, L. (2003). A reinforcement learning method based on adaptive simulated annealing. In *Proceedings International Midwest Symposium on Circuits and Systems (MWCAS), December 2003*, IEEE CAS, Cairo, Egypt. 121–124. `https://www.ingber.com/asa03_reinforce.pdf`.

Avellaneda, M., Stoikov, S. (2008). High-frequency trading in a limit order book. *Quantitative Finance* 8(3), 217–224.

Banaclocha, M., Bookkon, I., Banaclocha, H. (2010). Long-term memory in brain magnetite. *Medical Hypotheses* 74(2), 254–257.

Baradely, N., Bouchardz, B., Evangelista, D., Mounjid, O. (2018). Optimal inventory management and order book modeling. Technical Report arXiv:1802.08135v2 [q-fin.TR], Universite Paris-Dauphine, Paris.

Bartlett, G. (1988). Battle command training program. *Phalanx* 21, 18–20.

Bellinger, S. (2005). Modeling calcium wave oscillations in astrocytes. *Neurocomputing* 65(66), 843–850.

Binder, K., Stauffer, D. (1985). A simple introduction to monte carlo simulations and some specialized topics. In Binder, K. (Ed.), *Applications of the Monte Carlo Method in Statistical Physics*, Springer-Verlag, Berlin. 1–36.

Blanco, C. (2005). *Financial Risk Management: Beyond Normality, Volatility and Correlations*. Financial Economics Network, Waltham, MA. `http://www.fenews.com/fen46/front-sr/blanco/blanco.html`.

Bray, I., Gibson, A., White, J. (2020). Coronavirus disease 2019 mortality: a multivariate ecological analysis in relation to ethnicity, population density, obesity, deprivation and pollution. *Public Health* 185, 261–263. `https://doi.org/10.1016/j.puhe.2020.06.056`.

Burgarth, D., Facchi, P., Nakazato, H., Pascazio, S., Yuasa, K. (2018). Quantum zeno dynamics from general quantum operations. Technical Report arXiv:1809.09570v1 [quant-ph], Aberystwyth U., Aberystwyth, UK.

Cartea, A., Jaimungal, S., Ricci, J. (2014). Buy low sell high: a high frequency trading perspective. *SIAM Journal Financial Mathematics* 5(1), 415–444.

Cerny, V. (1982). A thermodynamical approach to the travelling salesman problem: An efficient simulation algorithm. Technical Report Report, Comenius University, Bratislava, Czechoslovakia.

Citi, L., Poli, R., Cinel, C. (2010). Documenting, modelling and exploiting P300 amplitude changes due to variable target delays in Donchin's speller. *Journal of Neural Engineering* 7(056006), 1–21. `https://dx.doi.org/10.1088/1741-2560/7/5/056006`.

Cont, R. (2011). Statistical modeling of high-frequency financial data. *IEEE Signal Processing* 28(5), 16–25.

Cont, R., Stoikov, S., Talreja, R. (2009). A stochastic model for order book dynamics. *Operations Research* 58(3), 1–21.

Conway, J., Kochen, S. (2006). The free will theorem. Technical Report arXiv:quant-ph/0604079 [quant-ph], Princeton U, Princeton, NJ.

Conway, J., Kochen, S. (2009). The strong free will theorem. *Notices of the American Mathematical Society* 56(2), 226–232.

Dekker, H. (1980). On the most probable transition path of a general diffusion process. *Physics Letters A* 80, 99–101.

Dionne, G., Duchesne, P., Pacurar, M. (2006). Intraday value at risk (IVAR) using tick-by-tick data with application to the toronto stock exchange. Technical Report Report, U de Montreal, Montreal. `http://www.fma.org/Stockholm/Papers/dionne_duchesne_pacurar.pdf`.

Dupuy, T. (1987). Can we rely on computer combat simulations? *Armed Forces Journal* August, 58–63.

Ericsson, K., Chase, W. (1982). Exceptional memory. *American Scientist* 70, 607–615.

Facchi, P., Lidar, D., Pascazio, S. (2004). Unification of dynamical decoupling and the quantum zeno effect. *Physical Review A* 69(032314), 1–6.

Facchi, P., Pascazio, S. (2008). Quantum zeno dynamics: mathematical and physical aspects. *Journal of Physics A* 41(493001), 1–45.

Fodra, P., Labadie, M. (2012). High-frequency market-making with inventory constraints and directional bets. Technical Report arXiv:1206.4810v1 [q-fin.TR], EXQIM, Paris.

Geman, S., Geman, D. (1984). Stochastic relaxation, gibbs distribution and the bayesian restoration in images. *IEEE Transactions Pattern Analysis Machine Intelligence* 6(6), 721–741.

Giacosa, G., Pagliara, G. (2014). Quantum zeno effect by general measurements. *Physical Review A* 052107, 1–5.

Goldberger, A., Amaral, L., Glass, L., Hausdorff, J., Ivanov, P., Mark, R., Mietus, J., Moody, G., Peng, C.K., Stanley, H. (2000). PhysioBank, PhysioToolkit, and PhysioNet: components of a new research resource for complex physiologic signals. *Circulation* 101(23), e215–e220. `http://circ.ahajournals.org/cgi/content/full/101/23/e215`.

Gueant, O. (2017). Optimal market making. Technical Report arXiv:1605.01862v5 [q-fin.TR], Universite Paris, Paris.

Hagan, S., Hameroff, S., Tuszynski, J. (2002). Quantum computation in brain microtubules: Decoherence and biological feasibility. *Physical Review E* 65(061901), 1–11. `http://link.aps.org/doi/10.1103/PhysRevE.65.061901`.

Hameroff, S., Penrose, R. (2013). Consciousness in the universe: A review of the 'Orch OR' theory. *Physics of Life Reviews* 403, 1–40. `https://dx.doi.org/10.1016/j.plrev.2013.08.002`.

Hick, W. (1952). On the rate of gains of information. *Quarterly Journal Experimental Psychology* 34(4), 1–33.

Horsewood, R. (2005). *Credit Correlation: Maths of All Angles*. Financial Economics Network, Waltham, MA. `http://www.fenews.com/fen39/euro_angles/euro_angles.html`.

Huang, W., Lehalle, C.A., Rosenbaum, M. (2014). Simulating and analyzing order book data: The queue-reactive model. Technical Report arXiv:1312.0563v2 [q-fin.TR], University Pierre et Marie Curie, Paris.

Ibragimon, R. (2005). Copula-based dependence characterizations and modeling for time series. Technical Report Report No. 2094, Harvard Institute Economic Research, Cambridge, MA. `http://post.economics.harvard.edu/hier/2005papers/HIER2094.pdf`.

Ingber, L. (1981). Towards a unified brain theory. *Journal Social Biological Structures* 4, 211–224. `https://www.ingber.com/smni81_unified.pdf`.

Ingber, L. (1982). Statistical mechanics of neocortical interactions. i. basic formulation. *Physica D* 5, 83–107. `https://www.ingber.com/smni82_basic.pdf`.

Ingber, L. (1983). Statistical mechanics of neocortical interactions. dynamics of synaptic modification. *Physical Review A* 28, 395–416. `https://www.ingber.com/smni83_dynamics.pdf`.

Ingber, L. (1984a). Statistical mechanics of neocortical interactions. derivation of short-term-memory capacity. *Physical Review A* 29, 3346–3358. `https://www.ingber.com/smni84_stm.pdf`.

Ingber, L. (1984b). Statistical mechanics of nonlinear nonequilibrium financial markets. *Mathematical Modelling* 5(6), 343–361. `https://www.ingber.com/markets84_statmech.pdf`.

Ingber, L. (1985). Statistical mechanics of neocortical interactions: Stability and duration of the 7+-2 rule of short-term-memory capacity. *Physical Review A* 31, 1183–1186. `https://www.ingber.com/smni85_stm.pdf`.

Ingber, L. (1989a). Very fast simulated re-annealing. *Mathematical Computer Modelling* 12(8), 967–973. `https://www.ingber.com/asa89_vfsr.pdf`.

Ingber, L. (1989b). Mathematical comparison of JANUS(T) simulation to national training center. In Johnson, S., Levis, A. (Eds.), *The Science of Command and Control: Part II, Coping With Complexity*, AFCEA International, Washington, DC. 165–176.

Ingber, L. (1990). Statistical mechanical aids to calculating term structure models. *Physical Review A* 42(12), 7057–7064. `https://www.ingber.com/markets90_interest.pdf`.

Ingber, L. (1991). Statistical mechanics of neocortical interactions: A scaling paradigm applied to electroencephalography. *Physical Review A* 44(6), 4017–4060. `https://www.ingber.com/smni91_eeg.pdf`.

Ingber, L. (1992). Generic mesoscopic neural networks based on statistical mechanics of neocortical interactions. *Physical Review A* 45(4), R2183–R2186. `https://www.ingber.com/smni92_mnn.pdf`.

Ingber, L. (1993a). Adaptive simulated annealing (ASA). Technical Report Global optimization C-code, Caltech Alumni Association, Pasadena, CA. `https://www.ingber.com/#ASA-CODE`.

Ingber, L. (1993b). Statistical mechanics of combat and extensions. In Jones, C. (Ed.), *Toward a Science of Command, Control, and Communications*, American Institute of Aeronautics and Astronautics, Washington, D.C. 117–149. ISBN 1-56347-068-3. `https://www.ingber.com/combat93_c3sci.pdf`.

Ingber, L. (1994). Statistical mechanics of neocortical interactions: Path-integral evolution of short-term memory. *Physical Review E* 49(5B), 4652–4664. `https://www.ingber.com/smni94_stm.pdf`.

Ingber, L. (1995). Statistical mechanics of multiple scales of neocortical interactions. In Nunez, P. (Ed.), *Neocortical Dynamics and Human EEG Rhythms*, Oxford University Press, New York, NY. 628–681. ISBN 0-19-505728-7. `https://www.ingber.com/smni95_scales.pdf`.

Ingber, L. (1996a). Canonical momenta indicators of financial markets and neocortical EEG. In Amari, S.I., Xu, L., King, I., Leung, K.S. (Eds.), *Progress in Neural Information Processing*, Springer, New York. 777–784. Invited paper to the 1996 International Conference on Neural Information Processing (ICONIP'96), Hong Kong, 24-27 September 1996. ISBN 981-3083-05-0. `https://www.ingber.com/markets96_momenta.pdf`.

Ingber, L. (1996b). Statistical mechanics of nonlinear nonequilibrium financial markets: Applications to optimized trading. *Mathematical Computer Modelling* 23(7), 101–121. `https://www.ingber.com/markets96_trading.pdf`.

Ingber, L. (1996c). Statistical mechanics of neocortical interactions: Multiple scales of EEG. In Dasheiff, R., Vincent, D. (Eds.), *Frontier Science in EEG: Continuous Waveform Analysis (Electroencephal. clin. Neurophysiol. Suppl. 45)*, Elsevier, Amsterdam. 79–112. Invited talk to Frontier Science in EEG Symposium, New Orleans, 9 Oct 1993. ISBN 0-444-82429-4. `https://www.ingber.com/smni96_eeg.pdf`.

Ingber, L. (1996d). Adaptive simulated annealing (ASA): lessons learned. *Control and Cybernetics* 25(1), 33–54. Invited paper to Control and Cybernetics on Simulated Annealing Applied to Combinatorial Optimization. `https://www.ingber.com/asa96_lessons.pdf`.

Ingber, L. (1997a). Statistical mechanics of neocortical interactions: Applications of canonical momenta indicators to electroencephalography. *Physical Review E* 55(4), 4578–4593. `https://www.ingber.com/smni97_cmi.pdf`.

Ingber, L. (1997b). *EEG Database*. UCI Machine Learning Repository, Irvine, CA. `http://archive.ics.uci.edu/ml/datasets/EEG+Database`.

Ingber, L. (1998a). Statistical mechanics of neocortical interactions: Training and testing canonical momenta indicators of EEG. *Mathematical Computer Modelling* 27(3), 33–64. `https://www.ingber.com/smni98_cmi_test.pdf`.

Ingber, L. (1998b). Data mining and knowledge discovery via statistical mechanics in nonlinear stochastic systems. *Mathematical Computer Modelling* 27(3), 9–31. `https://www.ingber.com/path98_datamining.pdf`.

Ingber, L. (1999). Statistical mechanics of neocortical interactions: Reaction time correlates of the g factor. *Psycholoquy* 10(068). Invited commentary on The g Factor: The Science of Mental Ability by Arthur Jensen. `https://www.ingber.com/smni99_g_factor.pdfandhttp://www.cogsci.ecs.soton.ac.uk/cgi/psyc/newpsy?10.068`.

Ingber, L. (2000). High-resolution path-integral development of financial options. *Physica A* 283(3-4), 529–558. `https://www.ingber.com/markets00_highres.pdf`.

Ingber, L. (2002). Statistical mechanics of portfolios of options. Technical Report Report 2002:SMPO, Physical Studies Institute, Chicago, IL. `https://www.ingber.com/markets02_portfolio.pdf`.

Ingber, L. (2005). Trading in risk dimensions (TRD). Technical Report Report 2005:TRD, Physical Studies Institute, Ashland, OR. `https://www.ingber.com/markets05_trd.pdf`.

Ingber, L. (2006a). Statistical mechanics of neocortical interactions: Portfolio of physiological indicators. Technical Report Report 2006:PPI, Physical Studies Institute, Ashland, OR. `https://www.ingber.com/smni06_ppi.pdf`.

Ingber, L. (2006b). Ideas by statistical mechanics (ISM). Technical Report Report 2006:ISM, Physical Studies Institute, Ashland, OR. `https://www.ingber.com/smni06_ism.pdf`.

Ingber, L. (2007a). Ideas by statistical mechanics (ISM). *Journal Integrated Systems Design and Process Science* 11(3), 31–54. `https://dl.acm.org/doi/abs/10.5555/1517398.1517402`.

Ingber, L. (2007b). Real options for project schedules (ROPS). Technical Report Report 2007:ROPS, Physical Studies Institute, Ashland, OR. `https://www.ingber.com/markets07_rops.pdf`.

Ingber, L. (2008a). Statistical mechanics of neocortical interactions (SMNI): testing theories with multiple imaging data. *NeuroQuantology Journal* 6(2), 97–104. `Invitedpaper.https://www.ingber.com/smni08_tt.pdf`.

Ingber, L. (2008b). AI and ideas by statistical mechanics (ISM). In Rabunal, J., Dorado, J., Pazos, A. (Eds.), *Encyclopedia of Artificial Intelligence*, Information Science Reference, New York. 58–64. ISBN 978-1-59904-849-9. `https://www.igi-global.com/chapter/ideas-statistical-mechanics/10226`.

Ingber, L. (2009a). Statistical mechanics of neocortical interactions: Portfolio of physiological indicators. *The Open Cybernetics Systemics Journal* 3(14), 13–26. `https://doi.org/10.2174/1874110x00903010013`.

Ingber, L. (2009b). Statistical mechanics of neocortical interactions: Nonlinear columnar electroencephalography. *NeuroQuantology Journal* 7(4), 500–529. `https://www.ingber.com/smni09_nonlin_column_eeg.pdf`.

Ingber, L. (2010a). Trading in risk dimensions. In Gregoriou, G. (Ed.), *The Handbook of Trading: Strategies for Navigating and Profiting from Currency, Bond, and Stock Markets*, McGraw-Hill, New York. 287–300.

Ingber, L. (2010b). Real options for project schedules (ROPS). *SGI Reflections International Journal of Science, Technology & Management* 2(2), 15–20. Invited paper. `http://sgi.ac.in/colleges/newsletters/1146080820111637301.pdf`.

Ingber, L. (2012a). Adaptive simulated annealing. In Oliveira, Jr., H., Petraglia, A., Ingber, L., Machado, M., Petraglia, M. (Eds.), *Stochastic global optimization and its applications with fuzzy adaptive simulated annealing*, Springer, New York. 33–61. Invited Paper. `https://www.ingber.com/asa11_options.pdf`.

Ingber, L. (2012b). Columnar EEG magnetic influences on molecular development of short-term memory. In Kalivas, G., Petralia, S. (Eds.), *Short-Term Memory: New Research*, Nova, Hauppauge, NY. 37–72. Invited Paper. `https://www.ingber.com/smni11_stm_scales.pdf`.

Ingber, L. (2012c). Influence of macrocolumnar EEG on ca waves. *Current Progress Journal* 1(1), 4–8. `https://www.ingber.com/smni12_vectpot.pdf`.

Ingber, L. (2015a). Calculating consciousness correlates at multiple scales of neocortical interactions. In Costa, A., Villalba, E. (Eds.), *Horizons in Neuroscience Research*, Nova, Hauppauge, NY. 153–186. ISBN 978-1-63482-632-7. Invited paper. `https://www.ingber.com/smni15_calc_conscious.pdf`.

Ingber, L. (2015b). Biological impact on military intelligence: Application or metaphor? *International Journal of Intelligent Defence Support Systems* 5(3), 173–185. `https://www.ingber.com/combat15_milint.pdf`.

Ingber, L. (2016a). Path-integral quantum PATHTREE and PATHINT algorithms. *International Journal of Innovative Research in Information Security* 3(5), 1–15. `https://www.ingber.com/path16_quantum_path.pdf`.

Ingber, L. (2016b). Statistical mechanics of neocortical interactions: Large-scale EEG influences on molecular processes. *Journal of Theoretical Biology* 395, 144–152. `https://www.ingber.com/smni16_large-scale_molecular.pdf~and~https://doi.org/10.1016/j.jtbi.2016.02.003`.

Ingber, L. (2017a). Evolution of regenerative ca-ion wave-packet in neuronal-firing fields: Quantum path-integral with serial shocks. *International Journal of Innovative Research in Information Security* 4(2), 14–22. `https://www.ingber.com/path17_quantum_pathint_shocks.pdf`.

Ingber, L. (2017b). Options on quantum money: Quantum path-integral with serial shocks. *International Journal of Innovative Research in Information Security* 4(2), 7–13. `https://www.ingber.com/path17_quantum_options_shocks.pdf`.

Ingber, L. (2017c). Quantum path-integral qPATHINT algorithm. *The Open Cybernetics Systemics Journal* 11, 119–133. `https://www.ingber.com/path17_qpathint.pdfandhttps://doi.org/10.2174/1874110X01711010119`.

Ingber, L. (2018a). Quantum calcium-ion interactions with EEG. *Sci* 1(7), 1–21. `https://www.ingber.com/smni18_quantumCaEEG.pdf~and~https://doi.org/10.3390/sci1010020`.

Ingber, L. (2018b). Quantum variables in finance and neuroscience. Technical Report Lecture Plates 2018:QVFN, Physical Studies Institute, Ashland, OR. `https://www.ingber.com/path18_qpathint_lecture.pdf`.

Ingber, L. (2018c). Quantum variables in finance and neuroscience II. Technical Report Report 2018:FNQV, Physical Studies Institute, Ashland, OR. `https://www.ingber.com/path18_qpathint.pdf`.

Ingber, L. (2020a). Developing bid-ask probabilities for high-frequency trading. *Virtual Economics* 3(2), 7–24. `https://www.ingber.com/markets19_bid_ask_prob.pdfandhttps://doi.org/10.34021/ve.2020.03.02(1)`.

Ingber, L. (2020b). Forecasting with importance-sampling and path-integrals. Technical Report Report 2020:FISPI, Physical Studies Institute, Ashland, OR. `https://www.ingber.com/asa20_forecast.pdfandhttps://doi.org/10.20944/preprints202009.0385.v1`.

Ingber, L. (2020c). Quantum calcium-ion affective influences measured by EEG. Technical Report Report 2020:QCIA, Physical Studies Institute, Ashland, OR. `https://www.ingber.com/quantum20_affective.pdf~and~https://doi.org/10.20944/preprints202009.0591.v1`.

Ingber, L., Chen, C., Mondescu, R., Muzzall, D., Renedo, M. (2001). Probability tree algorithm for general diffusion processes. *Physical Review E* 64(5), 056702–056707. `https://www.ingber.com/path01_pathtree.pdf`.

Ingber, L., Fujio, H., Wehner, M. (1991a). Mathematical comparison of combat computer models to exercise data. *Mathematical Computer Modelling* 15(1), 65–90. `https://www.ingber.com/combat91_data.pdf`.

Ingber, L., Mondescu, R. (2001). Optimization of trading physics models of markets. *IEEE Transactions Neural Networks* 12(4), 776–790. Invited paper for special issue on Neural Networks in Financial Engineering. `https://www.ingber.com/markets01_optim_trading.pdf`.

Ingber, L., Mondescu, R. (2003). Automated internet trading based on optimized physics models of markets. In Howlett, R., Ichalkaranje, N., Jain, L., Tonfoni, G. (Eds.), *Intelligent Internet-Based Information Processing Systems*, World Scientific, Singapore. 305–356. Invited paper. `https://www.ingber.com/markets03_automated.pdf`.

Ingber, L., Nunez, P. (1995). Statistical mechanics of neocortical interactions: High resolution path-integral calculation of short-term memory. *Physical Review E* 51(5), 5074–5083. `https://www.ingber.com/smni95_stm.pdf`.

Ingber, L., Nunez, P. (2010). Neocortical dynamics at multiple scales: EEG standing waves, statistical mechanics, and physical analogs. *Mathematical Biosciences* 229, 160–173. `https://www.ingber.com/smni10_multiple_scales.pdf`.

Ingber, L., Pappalepore, M., Stesiak, R. (2014). Electroencephalographic field influence on calcium momentum waves. *Journal of Theoretical Biology* 343, 138–153. `https://www.ingber.com/smni14_eeg_ca.pdfandhttps://doi.org/10.1016/j.jtbi.2013.11.002`.

Ingber, L., Srinivasan, R., Nunez, P. (1996). Path-integral evolution of chaos embedded in noise: Duffing neocortical analog. *Mathematical Computer Modelling* 23(3), 43–53. `https://www.ingber.com/path96_duffing.pdf`.

Ingber, L., Sworder, D. (1991). Statistical mechanics of combat with human factors. *Mathematical Computer Modelling* 15(11), 99–127. `https://www.ingber.com/combat91_human.pdf`.

Ingber, L., Wehner, M., Jabbour, G., Barnhill, T. (1991b). Application of statistical mechanics methodology to term-structure bond-pricing models. *Mathematical Computer Modelling* 15(11), 77–98. `https://www.ingber.com/markets91_interest.pdf`.

Ingber, L., Wilson, J. (1999). Volatility of volatility of financial markets. *Mathematical Computer Modelling* 29(5), 39–57. `https://www.ingber.com/markets99_vol.pdf`.

Ingber, L., Wilson, J. (2000). Statistical mechanics of financial markets: Exponential modifications to black-scholes. *Mathematical Computer Modelling* 31(8/9), 167–192. `https://www.ingber.com/markets00_exp.pdf`.

Innocenti, B., Parpura, V., Haydon, P. (2000). Imaging extracellular waves of glutamate during calcium signaling in cultured astrocytes. *Journal of Neuroscience* 20(5), 1800–1808.

Jensen, A. (1987). Individual differences in the hick paradigm. In Vernon, P. (Ed.), *Speed of Information-Processing and Intelligence*, Ablex, Norwood, NJ. 101–175.

Kirkpatrick, S., Gelatt, C., Vecchi, M. (1983). Optimization by simulated annealing. *Science* 220(4598), 671–680.

Kozlowski, W., Caballero-Benitez, S., Mekhov, I. (2015). Non-hermitian dynamics in the quantum zeno limit. Technical Report arXiv:1510.04857 [quant-ph], U Oxford, Oxford, UK.

Lallouette, J., Pitta, M.D., Berry, H. (2019). Astrocyte networks and intercellular calcium propagation. In *Computational Glioscience*, Springer, Cham, Switzerland. 177–210. `https://dx.doi.org/10.1007/978-3-030-00817-8_7`.

Laloux, L., Cizeau, P., Bouchaud, J., Potters, M. (1999). Noise dressing of financial correlation matrices. *Physical Review Letters* 83, 1467–1470.

Langouche, F., Roekaerts, D., Tirapegui, E. (1979). Discretization problems of functional integrals in phase space. *Physical Review D* 20, 419–432.

Langouche, F., Roekaerts, D., Tirapegui, E. (1982). *Functional Integration and Semiclassical Expansions*. Reidel, Dordrecht, The Netherlands.

Li, A., Hannah, T., Durbin, J., Dreher, N., McAuley, F., Marayati, N.F., Spiera, Z., Ali, M., Gometz, A., Kostman, J., Choudhri, T. (2020). Multivariate analysis of black race and environmental temperature on COVID-19 in the US. *The American Journal of the Medical Sciences* 360(4), 348–356. `https://doi.org/10.1016/j.amjms.2020.06.015`.

Litterman, R., Winkelmann, K. (1998). Estimating covariance matrices. Technical Report Report, Goldman Sachs, New York.

Ma, S. (1985). *Statistical Mechanics.* World Scientific, Philadelphia.

Majhi, S., Ghosh, D. (2018). Alternating chimeras in networks of ephaptically coupled bursting neurons. *Chaos* 28(083113). `https://doi.org/10.1063/1.5022612`.

Malevergne, Y., Sornette, D. (2002). General framework for a portfolio theory with non-gaussian risks and non-linear correlations. Technical Report Report, UCLA, Los Angeles, CA.

Mathews, J., Walker, R. (1970). *Mathematical Methods of Physics, 2nd ed.* Benjamin, New York, NY.

McKemmish, L., Reimers, J., McKenzie, R., Mark, A., Hush, N. (2009). Penrose-hameroff orchestrated objective-reduction proposal for human consciousness is not biologically feasible. *Physical Review E* 80(021912), 1–6. `http://link.aps.org/doi/10.1103/PhysRevE.80.021912`.

Metropolis, N., Rosenbluth, A., Rosenbluth, M., Teller, A., Teller, E. (1953). Equation of state calculations by fast computing machines. *Journal of Chemical Physics* 21(6), 1087–1092.

Muller, M., Gherardini, S., Caruso, F. (2016). Quantum zeno dynamics through stochastic protocols. Technical Report arXiv:1607.08871v1 [quant-ph], U Florence, Florence, Italy.

Murakami, S., Okada, Y. (2006). Contributions of principal neocortical neurons to magnetoencephalography and electroencephalography signals. *Journal of Physiology* 575(3), 925–936.

Nunez, P., Srinivasan, R. (2006). *Electric Fields of the Brain: The Neurophysics of EEG, 2nd Ed.* Oxford University Press, London.

Nunez, P., Srinivasan, R., Ingber, L. (2013). Theoretical and experimental electrophysiology in human neocortex: Multiscale correlates of conscious experience. In Pesenson, M. (Ed.), *Multiscale Analysis and Nonlinear Dynamics: From genes to the brain*, Wiley, New York. 149–178. `https://doi.org/10.1002/9783527671632.ch06`.

Okoli, C., Pawlowski, S. (2004). The delphi method as a research tool: an example, design considerations and applications. *Information and Management* 42(1), 15–29. `https://doi.org/10.1016/j.im.2003.11.002`.

Pasini, E., Bisulli, F., Volpi, L., Minardi, I., Tappata, M., Muccioli, L., Pensato, U., Riguzzi, P., Tinuper, P., Michelucci, R. (2020). EEG findings in COVID-19 related encephalopathy. *Clinical Neurophysiology* 131(9), 2265–2267. `https://doi.org/10.1016/j.clinph.2020.07.003`.

Patil, Y., Chakram, S., Vengalattore, M. (2015). Measurement-induced localization of an ultracold lattice gas. *Physical Review Letters* 115(140402), 1–5. `http://link.aps.org/doi/10.1103/PhysRevLett.115.140402`.

Pereira, Jr., A., Furlan, F. (2009). On the role of synchrony for neuron-astrocyte interactions and perceptual conscious processing. *Journal of Biological Physics* 35(4), 465–480.

Pincus, M. (1970). A monte carlo method for the approximate solution of certain types of constrained optimization problems. *Operations Research* 18, 1225–1228.

Preskill, J. (2015). Quantum mechanics. Technical Report Lecture Notes, Caltech, Pasadena, CA. `http://www.theory.caltech.edu/people/preskill/ph219/`.

Reyes, R., Parpura, V. (2009). The trinity of Ca2+ sources for the exocytotic glutamate release from astrocytes. *Neurochemistry International* 55(3), 1–14.

Rosenberg, J., Schuermann, T. (2004). A general approach to integrated risk management with skewed, fat-tailed risks. Technical Report Staff Report No. 185, Fed. Res. Bank NY, New York, NY.

Ross, W. (2012). Understanding calcium waves and sparks in central neurons. *Nature Reviews Neuroscience* 13, 157–168.

Salazar, R., Dotson, N., Bressler, S., Gray, C. (2012). Content-specific fronto-parietal synchronization during visual working memory. *Science* 338(6110), 1097–1100. `https://dx.doi.org/10.1126/science.1224000`.

Scemes, E., Giaume, C. (2006). Astrocyte calcium waves: What they are and what they do. *Glia* 54(7), 716–725. `https://dx.doi.org/10.1002/glia.20374`.

Schulman, L. (1981). *Techniques and Applications of Path Integration.* J. Wiley & Sons, New York.

Schulten, K. (1999). Quantum mechanics. Technical Report Lecture Notes, U. Illinois, Urbana, IL. `http://www.ks.uiuc.edu/Services/Class/PHYS480/`.

Szu, H., Hartley, R. (1987). Fast simulated annealing. *Physics Letters A* 122(3-4), 157–162.

vanCreveld, M. (1985). *Command in War.* Harvard University Press, Cambridge, MA.

vanLaarhoven, P., Aarts, E. (1987). *Simulated Annealing: Theory and Applications.* D. Reidel, Dordrecht, The Netherlands.

Volterra, A., Liaudet, N., Savtchouk, I. (2014). Astrocyte Ca2+ signalling: an unexpected complexity. *Nature Reviews Neuroscience* 15, 327–335.

Wehner, M., Wolfer, W. (1983a). Numerical evaluation of path-integral solutions to fokker-planck equations. I. *Physical Review A* 27, 2663–2670.

Wehner, M., Wolfer, W. (1983b). Numerical evaluation of path-integral solutions to fokker-planck equations. II. restricted stochastic processes. *Physical Review A* 28, 3003–3011.

Wehner, M., Wolfer, W. (1987). Numerical evaluation of path integral solutions to fokker-planck equations. III. time and functionally dependent coefficients. *Physical Review A* 35, 1795–1801.

Wu, S., Wang, L., Yi, X. (2012). Time-dependent decoherence-free subspace. *Journal of Physics A* 405305, 1–11.

Zhang, G., Simon, H. (1985). STM capacity for chinese words and idioms: Chunking and acoustical loop hypotheses. *Memory & Cognition* 13, 193–201.